
Supplementary information

Thermal chiral anomaly in the magnetic-field-induced ideal Weyl phase of $\text{Bi}_{1-x}\text{Sb}_x$

In the format provided by the authors and unedited

Supplement: Thermal chiral anomaly in the magnetic-field induced ideal Weyl phase of $\text{Bi}_{1-x}\text{Sb}_x$

Dung Vu¹, Wenjuan Zhang², Cüneyt Şahin^{3,4}, Michael E. Flatté^{3,4}, Nandini Trivedi², Joseph P. Heremans^{1,2,5}

1. Department of Mechanical and Aerospace Engineering, The Ohio State University, Columbus, Ohio 43210
2. Department of Physics, The Ohio State University, Columbus, Ohio 43210
3. Optical Science and Technology Center and Department of Physics and Astronomy, The University of Iowa, Iowa City, Iowa 52242
4. Pritzker School of Molecular Engineering, University of Chicago, Chicago, Illinois 60637
5. Department of Material Science and Engineering, The Ohio State University, Columbus, Ohio 43210

Content:

- S1. The Wiedemann Franz Law in semi-classical and extreme-quantum limits.
- S2. The modified virtual crystal approximation model used to calculate the g -tensors, and experimental validation.
- S3. The Berry curvature calculation, the Fukui method, and the location of Weyl points in the Brillouin Zone.
- S4. Single-crystal growth and structural characterization.
- S5. Sample characterization: Hall effect, magnetoresistance and thermal conductivity.
- S6 Error analysis of thermal conductivity measurements.
- S7 Thermal conductivity κ_{zz} measurements along the trigonal direction.
- S8. Angular dependence of $\kappa_{zz}(H_z)$
- S9. Test of $\kappa_{zz}(H_z)$ for surface effect.
- S10 Reproducibility of the determination of the Wiedemann-Franz law and error analysis.

S1. The Wiedemann Franz Law in semi-classical and extreme-quantum limits

The Wiedemann-Franz law (WFL) is a statement about the ratio of the longitudinal thermal conductivity κT to the longitudinal electrical conductivity σ , quantified by the Lorenz ratio $L \equiv \kappa / \sigma T$. In a free-electron metal, $L = L_0 \equiv \pi^3 / 3 \left(k_B / e \right)^2$ ($L_0 = 2.4 \times 10^{-8} (\text{V/K})^2$), if the scattering time of electrons in electrical and thermal conductivity are identical. There are two aspects of violation of the WFL, corresponding to two questions. (1) Is the Lorenz ratio L temperature dependent? (2) Is its value equal to the free-electron value L_0 ? We discuss these questions in the semi-classical and extreme-quantum limits (EQL) of a Weyl semimetal in an external magnetic field, and consider the case of ambipolar thermal conductivity, which can become important in semimetals and intrinsic semiconductors.

From Onsager's generalized transport equations, the flux vectors of charge (\mathbf{J}^e) and heat (\mathbf{J}^Q) are related to the electric field (\mathbf{E}) and temperature gradient by:

$$\begin{pmatrix} \mathbf{J}^e \\ \mathbf{J}^Q \end{pmatrix} = \begin{pmatrix} \boldsymbol{\sigma} & \boldsymbol{\alpha} \\ -\boldsymbol{\alpha} T & \boldsymbol{\kappa}_0 \end{pmatrix} \begin{pmatrix} \mathbf{E} \\ -\nabla T \end{pmatrix} \quad (\text{S1.1})$$

where $\boldsymbol{\sigma}$, $\boldsymbol{\alpha}$, and $\boldsymbol{\kappa}_0$ are the electrical conductivity, thermoelectric conductivity, and thermal conductivity tensors, respectively. With the electric field and thermal gradient applied along the z direction, and upon imposing the boundary condition that no current flows in or out of the sample, $0 = J_z^e = \sigma_{zz} E_z + \alpha_{zz} (-\nabla_z T)$, we obtain an induced thermoelectric field

$$E_z^{ind} = - \left(\alpha_{zz} / \sigma_{zz} \right) (-\nabla_z T) \text{ in the opposite direction of the thermal gradient to prevent the electric}$$

current flow. The quantity $S \equiv \left(\frac{\alpha_{zz}}{\sigma_{zz}} \right)$ is the Seebeck coefficient. The total open-circuit

thermal conductivity then is given by:

$$\kappa_{zz} \equiv \frac{J_z^Q}{(-\nabla_z T)} = \kappa_{zz,0} + \frac{\alpha_{zz}^2 T}{\sigma_{zz}} = \kappa_{zz,0} + S^2 \sigma T \quad (\text{S1.2})$$

as reported in the main text. Here, the first two indices indicate the direction of the applied field and the induced current. The second term in Eq. (S1.2) is the ambipolar thermal conductivity $\kappa_A = S^2 \sigma T$. We see that the WFL can be violated if: (a) S or α_{zz} is finite because the WFL holds only for $\kappa_{zz,0}$; in this case, $L > L_0$; or (b) $S = 0$ or $\alpha_{zz} = 0$, but different scattering mechanisms limit κ (often dominated by inelastic scattering, which is temperature dependent) and σ (often dominated by momentum or elastic scattering). This gives $L < L_0$. In classical materials, L ranges¹ from 0.5 to 2.6×10^{-8} (V/K)², or slightly more for semimetals.

From the Boltzmann equation, we obtain the longitudinal magneto-thermal $\kappa_{zz,z}$, magneto-electrical $\sigma_{zz,z}$, and magneto-thermoelectrical $\alpha_{zz,z}$ conductivities^{2,3} (here, the third index is the direction of the applied magnetic field), given by:

$$\begin{aligned} \kappa_{zz,z} &= \int \frac{d^3 \mathbf{k}}{(2\pi)^3} D(\mathbf{B}, \boldsymbol{\Omega}) \tau \left(v_z + \frac{eB_z}{\hbar} \boldsymbol{\Omega} \cdot \mathbf{v} \right)^2 \left(-\frac{\partial f_0}{\partial \varepsilon} \right) \frac{(\varepsilon - \mu)^2}{T} \\ \sigma_{zz,z} &= e^2 \int \frac{d^3 \mathbf{k}}{(2\pi)^3} D(\mathbf{B}, \boldsymbol{\Omega}) \tau \left(v_z + \frac{eB_z}{\hbar} \boldsymbol{\Omega} \cdot \mathbf{v} \right)^2 \left(-\frac{\partial f_0}{\partial \varepsilon} \right) \\ \alpha_{zz,z} &= e \int \frac{d^3 \mathbf{k}}{(2\pi)^3} D(\mathbf{B}, \boldsymbol{\Omega}) \tau \left(v_z + \frac{eB_z}{\hbar} \boldsymbol{\Omega} \cdot \mathbf{v} \right)^2 \left(-\frac{\partial f_0}{\partial \varepsilon} \right) \frac{\varepsilon - \mu}{T} \end{aligned} \quad (\text{S1.3})$$

where μ is the chemical potential and $D(\mathbf{B}, \boldsymbol{\Omega}) = \left[1 + \left(\frac{e}{\hbar} \right) \mathbf{B} \cdot \boldsymbol{\Omega} \right]^{-1}$ arises due to the modification of the phase space in an external magnetic field. Eq. (S1.3) is written assuming that the same

relaxation time τ governs the thermal and electrical conductivity. Further, we assume that τ^{-1} is the inter-Weyl-point scattering probability.

We show below that in an ideal WSM with the chemical potential at the Weyl points ($\mu=0$) in the EQL, $\alpha_{zz}=0$ and the WFL holds with the free-electron Lorenz number $L=L_0$. In the semi-classical regime at $B=0$, on the other hand, the Lorenz number for $\mu=0$ is different from the free-electron value: $L>L_0$ at temperatures below the band width of the Weyl bands. With increasing T , due to contributions from non-linear parts of the electronic structure, the Lorenz ratio decreases towards L_0 . Further, at low T if $\mu\neq 0$, the Lorenz ratio L shows a linear B dependence only in the semi-classical regime, arising from a non-zero Seebeck coefficient and ambipolar thermal conductivity that depends linearly on the magnetic field, which leads to a violation of the WFL.

(1) Extreme-quantum limit:

In the EQL, the energy dispersion for the n^{th} Landau level is given by:

$$\varepsilon_n(k_z) = \begin{cases} \pm \hbar v \sqrt{2|n|\ell_B^{-2} + k_z^2}, & n \neq 0 \\ \chi \hbar v k_z, & n = 0 \end{cases} \quad (\text{S1.4})$$

where $\ell_B \equiv \sqrt{\hbar/eB}$ is the magnetic length, v is the Fermi velocity, and χ is the chirality of the Weyl node. This implies that the $n=0$ Landau level disperses in opposite directions at the two nodes. The density of states for the $n=0$ Landau level is given by:

$$\mathcal{D}(\varepsilon) = \int \frac{d^3\mathbf{k}}{(2\pi)^3} \delta(\varepsilon - \varepsilon_{\mathbf{k}}) = \frac{1}{(2\pi)^2 \hbar v \ell_B^2} = \frac{eB}{4\pi^2 \hbar^2 v} \quad (\text{S1.5})$$

using which we obtain the following results for the transport coefficients in the EQL at $\mu=0$:

$$\begin{aligned}
\kappa_{zz,z}^{EQ} &= N_w \int d\varepsilon \mathcal{D}(\varepsilon) \tau v^2 \left(-\frac{\partial f_0}{\partial \varepsilon} \right) \frac{(\varepsilon - \mu)^2}{T} = N_w \frac{e B_z v \tau (k_B T)^2}{4\pi^2 \hbar^2 T} I_2 = N_w \frac{e v \tau k_B^2}{4\pi^2 \hbar^2} \frac{\pi^2}{3} T B_z \\
\sigma_{zz,z}^{EQ} &= N_w e^2 \int d\varepsilon \mathcal{D}(\varepsilon) \tau v^2 \left(-\frac{\partial f_0}{\partial \varepsilon} \right) = N_w \frac{e^3 B_z v \tau}{4\pi^2 \hbar^2} I_0 = N_w \frac{e^3 v \tau}{4\pi^2 \hbar^2} B_z \\
\alpha_{zz,z}^{EQ} &= N_w e \int d\varepsilon \mathcal{D}(\varepsilon) \tau v^2 \left(-\frac{\partial f_0}{\partial \varepsilon} \right) \frac{\varepsilon - \mu}{T} = N_w \frac{e^2 B_z v \tau k_B}{4\pi^2 \hbar^2} I_1 = 0
\end{aligned} \tag{S1.6}$$

with:

$$I_m \equiv \int_{-\infty}^{\infty} x^m \left(-\frac{\partial f_0}{\partial x} \right) dx = \begin{cases} 1, & m = 0 \\ 0, & m = \text{odd} \\ 2m\Gamma(m)\zeta(m)(1-2^{1-m}), & m \neq 0, m = \text{even} \end{cases} \tag{S1.7}.$$

Here $m \in \{0, 1, 2, \dots\}$, the number of Weyl points is N_w , the velocity along the z -axis is

$v_z = \frac{\partial \varepsilon_{\mathbf{k}}}{\hbar \partial k_z} = v$, the reduced energy scale is $x \equiv (\varepsilon - \mu) / k_B T$, the Fermi-Dirac distribution is

$f_0 = \{1 + \exp(x)\}^{-1}$, the gamma function is $\Gamma(m)$, and the Riemann-zeta function is $\zeta(m)$. In this

regime, we find that the WFL holds for the chiral $n = 0$ Landau level:

$$L = \left(\frac{k_B}{e} \right)^2 \left[\frac{I_2}{I_0} \right] = \frac{\pi^2}{3} \left(\frac{k_B}{e} \right)^2 = L_0 \tag{S1.8}.$$

When chemical potential is set at the energy of Weyl points ($\mu = 0$), α , S , and thus, the ambipolar thermal conductivity vanish identically.

Note that when the inelastic scattering time of electrons that enters the thermal conductivity is τ_{eff} such that $\tau_{eff}^{-1} = \tau^{-1} + \tau_{\varepsilon}^{-1}$, where τ_{ε} is the inelastic scattering time, the Lorenz ratio is reduced by the ratio⁴ τ_{eff} / τ , and $L < L_0$.

(2) The semi-classical regime:

At $B = 0$ and for a linear dispersion:

$$\varepsilon_{\mathbf{k}} = \pm \hbar v |\mathbf{k} - \mathbf{k}_w| \quad (\text{S1.9})$$

around the Weyl nodes at $\pm \mathbf{k}_w$, we obtain the density of states:

$$\mathcal{D}(\varepsilon) = \frac{\varepsilon^2}{2\pi^2 (\hbar v)^3} \quad (\text{S1.10}).$$

Assuming an energy-independent scattering time τ , we obtain at $\mu = 0$

$$\begin{aligned} \kappa_{zz} &= N_w \frac{\tau (k_B T)^4}{2\pi^2 \hbar^3 v T} I_4 = N_w \frac{7\pi^2}{30} \frac{\tau k_B^4}{\hbar^3 v} T^3 \\ \sigma_{zz} &= N_w \frac{e^2 \tau}{2\pi^2 \hbar^3 v} (k_B T)^2 I_2 = N_w \frac{1}{6} \frac{e^2 \tau k_B^2}{\hbar^3 v} T^2 \\ \alpha_{zz} &= N_w \frac{e\tau}{2\pi^2 \hbar^3 v} (k_B T)^3 I_3 = 0 \end{aligned} \quad (\text{S1.11}).$$

We find that the Lorentz ratio then is given by:

$$L = \left(\frac{k_B}{e} \right)^2 \left[\frac{I_4}{I_2} \right] = \frac{7\pi^2}{5} \left(\frac{k_B}{e} \right)^2 \quad (\text{S1.12}).$$

Thus, in an ideal Weyl semimetal at zero field, the Lorentz ratio is a constant, but deviates from the free-electron value; however, in the EQL, it recovers the free-electron value.

These conclusions are based on the fact that the Fermi integrals can be solved analytically in the cases discussed. This is unlike the case of the factor $\pi^2/3$ that shows up in the Mott relation for the thermopower of degenerate semiconductors and metals; there, it is the result of a Bethe-Sommerfeld expansion.

S2. The modified virtual crystal approximation model used to calculate the g -tensors, and experimental validation.

The evolution of $\text{Bi}_{1-x}\text{Sb}_x$ alloys shown in Fig. 1 of the main text is based on calculations made using the tight-binding (TB) model. As explained in Fig. 1, in zero magnetic field, $\text{Bi}_{1-x}\text{Sb}_x$ alloys are conventional semimetals for $x < \sim 7.7$ at.% and become topological insulators (TI) for $x > 8.8$ at.%. In a trigonal magnetic field $H_z // \langle 001 \rangle$, the direct band gap at the L-point of the Brillouin Zone (BZ) is calculated first to close with H_z , then invert at high values of H_z , forming a Weyl semimetal (WSM). Here, we outline the TB model used to calculate the band closing and then validate it experimentally using magnetic-field-dependent Hall data on the TI regime.

The TB Hamiltonian of Ref. [5] predicts band parameters, electronic structure, and effective masses correctly. However, interpolating these TB parameters linearly in a virtual crystal approximation (VCA) for a Bi-Sb alloy such as

$$V_{\text{Alloy}}(lmn) = (1-x)V_{\text{Bi}}(lmn) + xV_{\text{Sb}}(lmn) \quad (\text{S2.1})$$

does not produce the correct ordering and behavior of the band edges at the L- and T-points. As shown in Fig. S2(a), the linear VCA results in a band crossing of L-points at an antimony concentration of $\sim 3\%$ without a band inversion. In this model, an incorrect inversion occurs at a composition that is beyond the semimetal-semiconductor transition. Ref. [6] describes another approach to overcome this discrepancy with an alternative VCA:

$$V_{\text{alloy}}(lmn) = (1-x^2)V_{\text{Bi}}(lmn) + xV_{\text{Sb}}(lmn) \quad (\text{S2.2}).$$

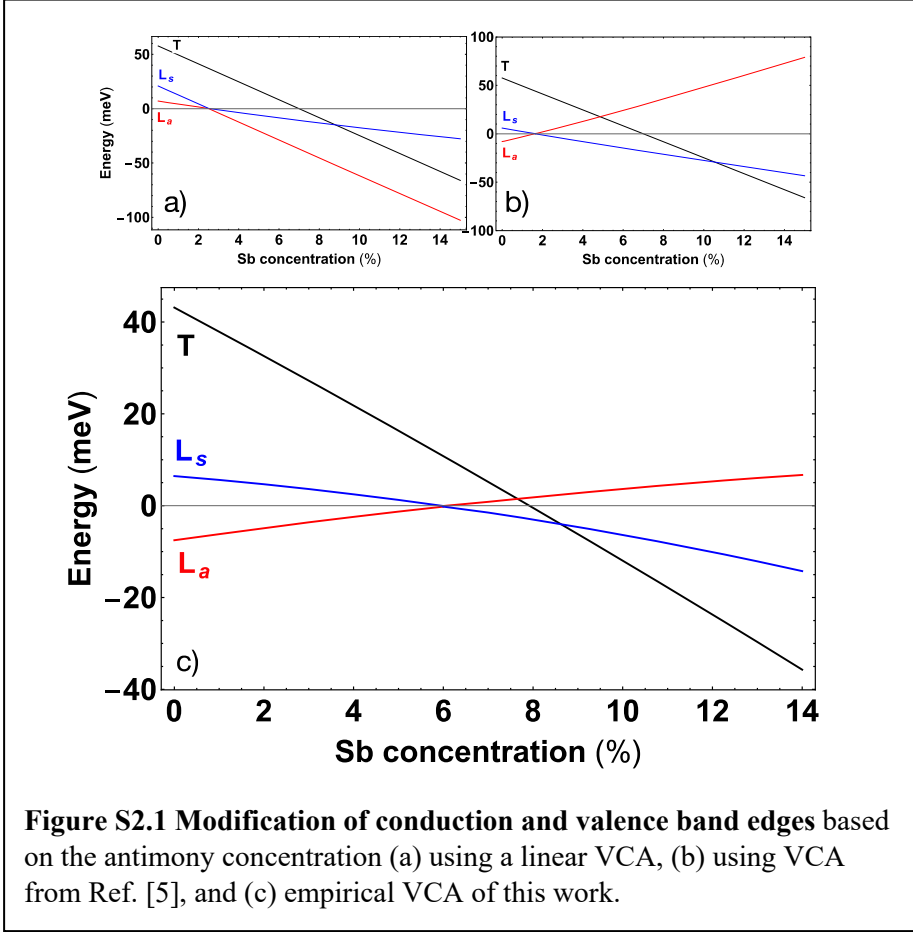


Figure S2.1 Modification of conduction and valence band edges based on the antimony concentration (a) using a linear VCA, (b) using VCA from Ref. [5], and (c) empirical VCA of this work.

This approach correctly describes the band inversion between L_a and L_s . However, it cannot reproduce the correct compositions at which band crossings are located, or the experimentally known band gaps occurring at certain concentrations, as shown in Fig S2.1(b). Here, we propose a non-linear empirical VCA:

$$V_{\text{alloy}}(lmn) = (1-x)V_{\text{Bi}}(lmn) + xV_{\text{Sb}}(lmn) + x(1-x)\alpha(lmn) \quad (\text{S2.3}),$$

and find the values of the α fitting parameters for each TB parameter fitting the experimental

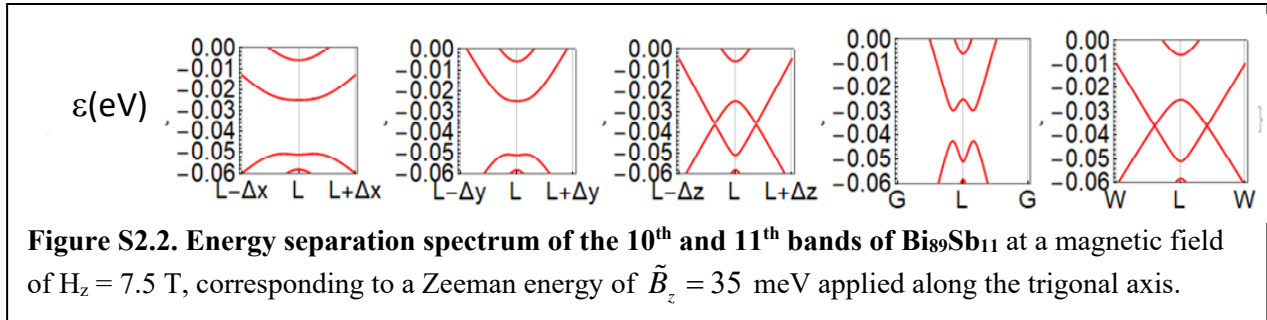
measurements. The lattice parameters of the BiSb alloys are shown to follow the Vegard's rule up to 30%.^{7,8} As such, the structural parameters, such as lattice constants, atomic distances, relative positions of the two basis

Parameter	(eV)	Parameter	(eV)
$\alpha_{\text{ss}\sigma,1}$	3	$\alpha_{\text{ss}\sigma,2}$	-3
$\alpha_{\text{sp}\sigma,1}$	0.06	$\alpha_{\text{sp}\sigma,2}$	0.06
$\alpha_{\text{pp}\sigma,1}$	-0.015	$\alpha_{\text{pp}\sigma,2}$	0.015
$\alpha_{\text{pp}\pi,1}$	0.08	$\alpha_{\text{pp}\pi,2}$	-0.08
α_0	0.6		

Table S2.1 VCA parameters of BiSb alloys: α_0 is for on-site energies and subscripts 1 and 2 indicate first- and second-nearest neighbors.

atoms in the conventional hexagonal cell, and primitive and reciprocal lattice vectors, are modified with a linear VCA. We also use a linear VCA for spin-orbit couplings and the third-nearest-neighbor overlap integrals, which do not affect the band structure significantly. We

observe that changing the first- and second-nearest-neighbor parameters results in reordering of the bands that originate from $ss\sigma$, $pp\sigma$, and $pp\pi$ orbitals, but not of the $sp\sigma$ ones. Furthermore, we observe that different TB parameters have different effects on the band structure evolution. For instance, sigma bonds ($ss\sigma$ and $pp\sigma$) shift the concentration of x at which L_s and L_a bands intersect, whereas the slope of the T-band is affected mostly by a change in pi bonds ($pp\pi$). Moreover, the slopes of the L_s - and L_a -bands depend on the sigma bonds between s - and p -orbitals ($sp\sigma$). We report the parameters of the nonlinear empirical VCA in Table S2. The band structure resulting from this VCA indicates that the band gap at 5% Sb is 3 meV, and the band gap at 12% Sb is 15 meV as shown in Fig. S2 (c). The intersection between L_a and L_s , between L_a and T, and between L_s and T are located at 6%, 7.7%, and 8.6% respectively.⁹



Following the calculation of the band edges with our new VCA, we compute g -tensors and the modification of the bands under an external magnetic field. The energy spectrum of the bands from 9 to 12 (the two highest valence and two lowest conduction bands) is given in Fig. S2.2. The bandwidth (the overlap between the bands) is $E_{BW} = 35$ meV at 7.5 T for $x=10.5\%$. In slightly different concentrations ranging from 10.5% to 15.1%, we observe that the bandwidth varies between 35 meV and 19 meV. The sensitivity of the energy overlap to the Sb content is then the same as that of the direct L-point gap, of order of $dE_{BW}/dx \sim 3$ meV per 1% of Sb in the alloy, assuming that the g factor is not very field dependent and the band edge energies vary

linearly with x . Consequently, the bandwidth is calculated to be $E_{BW} = 20$ meV at 7.5 T for $x=15.1\%$. The calculated Fermi velocity is $v_F = 4.0 \times 10^5$ m/s at 5 T and 5.0×10^5 m/s at 8 T.

We can check qualitatively the closing of the direct energy gap at L-point in the magnetic-field range where $\text{Bi}_{89}\text{Sb}_{11}$ is a semiconductor by measuring the magnetic-field-dependent Hall concentration as a function of temperature. For Hall resistivity, we use the notation $\rho_{xy}(H_z)$, where x is the index of the direction of the voltage measured, y is the direction of the applied current, and z is the direction of the applied magnetic field. Here, we measure $\rho_{xy}(H_z)$ with x along the binary direction [100], y along the bisectrix direction [010], and z along the trigonal direction [001]. This approach only holds when the Hall effect measurement correctly represents the excess carrier concentration, the difference between the density of electrons and that of holes, i.e., when

$$n(T, H_z) = \frac{1}{e \left(\frac{d\rho_{xy}(H_z)}{dH_z} \right)} \quad (\text{S2.4}).$$

This approach does not hold when the Hall effect becomes dominated by multi-carrier effects,¹⁰ which occurs in the presence of both electrons and holes in near-equal concentrations. Here, this is the case either in the semimetallic regime at higher magnetic fields, or

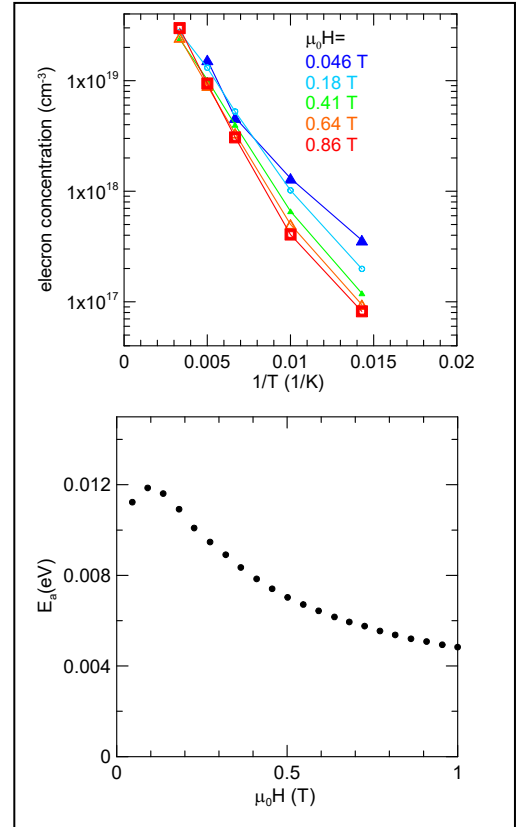


Figure S2.3 $\text{Bi}_{89}\text{Sb}_{11}$ Hall carrier concentration and activation energy. (top) $n(T, H_z)$ measured at the indicated H_z values plotted versus the inverse temperature. (bottom) Field dependence of the thermal activation energy E_a of $n(T, H_z)$ between 60 and 100 K. The Hall effect at higher magnetic fields does not reflect n accurately, resulting in a positive curvature above 0.3 T.

once the temperature is high enough that the material is a semiconductor with thermally excited intrinsic electrons and holes. This becomes the case at fields above about 0.5 T and when $E_g(H_z) < k_B T$. Measurements of $\rho_{xy}(H_z)$ at $\mu_0 H_z < 0.047$ T are used with Eq. (S2.4) to calculate the concentrations and mobilities shown in Fig. 2 and reported in Table 1. Here, in contrast, values for $n(T, H_z)$ derived from Eq. (S2.4) at various values of H_z are plotted versus $1/T$ in Fig. S2.3 (top). An Arrhenius function

$$n(T, H_z) = n_0(H_z) e^{-E_a(H_z)/k_B T} \quad (\text{S2.5})$$

can be fit through the data between 60 and 100 K, giving a field-dependent value for the thermal activation energy $E_a(H_z)$. The resulting values are shown in Fig. S2.3 (bottom), which displays a clear decrease in E_a with field H_z . The band calculations predict E_a , which is related to E_g , to decrease linearly with H_z since the gap closing is due to a Zeeman energy term. While the decrease is observed, the linearity with H_z is not. This is because with increasing H_z , the Hall data include more multi-carrier effects¹⁰ and Eq. (S2.4) becomes less accurate. Nevertheless, Fig. S2.3 shows that the gap closes with H_z .

S3. The Berry curvature calculation, the Fukui method, and the location of Weyl points in the Brillouin Zone.

The Berry curvature, $\mathbf{\Omega}_n(\mathbf{k}) = \nabla_{\mathbf{k}} \times \mathbf{A}_n(\mathbf{k})$, is a gauge-invariant geometrical quantity that can be obtained from the Berry connection $A_n(\mathbf{k}) = i \langle n(\mathbf{k}) | \nabla_{\mathbf{k}} | n(\mathbf{k}) \rangle$, the analog of the electromagnetic vector potential. The two Weyl points (WP) each carry the Berry curvature of a monopole $\mathbf{\Omega}(\mathbf{k}) = \chi \mathbf{k}/k^3$ with opposite chirality of $\chi = \pm 1$. The Chern number is obtained by integrating the Berry curvature, $\gamma_n = \int d\mathbf{S} \cdot \mathbf{\Omega}_n(\mathbf{k})$, over a closed surface, the BZ, and is related to the Berry phase γ_n through the relation $c_n = \gamma_n / 2\pi$. A numerical calculation of the Chern numbers is carried starting from a multiplet of wave vectors $\psi = (|n_1\rangle, \dots, |n_{10}\rangle)$, eigenfunctions of H . The Berry curvature \tilde{F} is calculated following Ref. [11] and using their notation to make the distinction between the discretized \tilde{F} and the Berry curvature $\mathbf{\Omega}$ in continuum. The Chern number $\tilde{c}_n = (2\pi i)^{-1} \sum_1 \tilde{F}(k_1)$ of n^{th} band is determined from \tilde{F} , and the total Chern number is obtained by summing the Chern numbers of all filled bands up to $n=10$. Numerically, this is done by integrating \tilde{F} in the (G_1, G_2) plane (Fig. 1(k), main text) while sweeping along the G_1 axis. An integer change in the Chern number, which constitutes the evidence for a change of the topology and existence of the WPs, is detected in a pair of points separated symmetrically near each L-point in the 3D BZ (Fig. S3.1). WPs are located by determining the locations of the Berry curvature monopoles and nodes with opposite chirality $\chi = \pm 1$; their position is given schematically in Fig. 1(j) (main text) and precisely hereunder. To find the monopoles of Berry curvature, i.e. the WPs, we must determine the distribution of Berry curvature in k -space. This is done most efficiently using the Fukui¹¹ numerical method described in the following steps:

(1) We use as a reference frame the reciprocal lattice vectors $\mathbf{G} = (\mathbf{G}_1, \mathbf{G}_2, \mathbf{G}_3)$ along the Γ -L lines shown in Fig. 2(k) (main text). We fix the fraction along the direction $\mathbf{G}_3 - k_3 \cdot \mathbf{G}_3$ where $k_3 \in [0, 1]$ and discretize the 2D BZ spanned by reciprocal lattice vectors $(\mathbf{G}_1 \times \mathbf{G}_2)$ into small $\delta\mathbf{G}_1 \times \delta\mathbf{G}_2$ patches, where $\{\mathbf{k}_l\}$ are the k-points.

(2) Next, we calculate the Berry flux through each small patch as

$$\tilde{F}(\mathbf{k}_l) = \ln U_1(\mathbf{k}_l) U_2(\mathbf{k}_l + \delta\mathbf{G}_1) U_1^{-1}(\mathbf{k}_l + \delta\mathbf{G}_2) U_2^{-1}(\mathbf{k}_l) \quad (\text{S3.1})$$

where $U_i(\mathbf{k}_l)$ is a link variable, which gives the phase acquired by the wave function of the n th band as an electron moves from \mathbf{k}_l to $\mathbf{k}_l + \delta\mathbf{G}_i$ given by: (index $i = 1, 2$)

$$U_i(\mathbf{k}_l) = \frac{\det \psi^\dagger(\mathbf{k}_l) \psi(\mathbf{k}_l + \delta\mathbf{G}_i)}{|\det \psi^\dagger(\mathbf{k}_l) \psi(\mathbf{k}_l + \delta\mathbf{G}_i)|} \quad (\text{S3.2})$$

(3) Finally, we compute the sum of the Berry flux through each patch to obtain the lattice Chern number for the n th band: $\tilde{c}_n = (2\pi i)^{-1} \sum_l \tilde{F}(\mathbf{k}_l)$.

The WPs are centered around the L-points of the BZ. The separation found from the Berry curvature plot (see Fig. 1(k) in the main text and Fig. S2.2), is mainly along field direction (z), with a minor contribution along the Γ -L direction. The coordinates for the separation (1/2 on either side of each L-point) at $H_z = 8$ T for the upper half of the BZ are: (0.678, 0.520, 0.520), (0.520, 0.678, 0.520), (0.520, 0.520, 0.678), in the $\mathbf{G}(\mathbf{G}_1, \mathbf{G}_2, \mathbf{G}_3)$ axis system, where (0, 0, 0) is the Γ -point and (0.5, 0, 0) is the L-point along \mathbf{G}_1 .

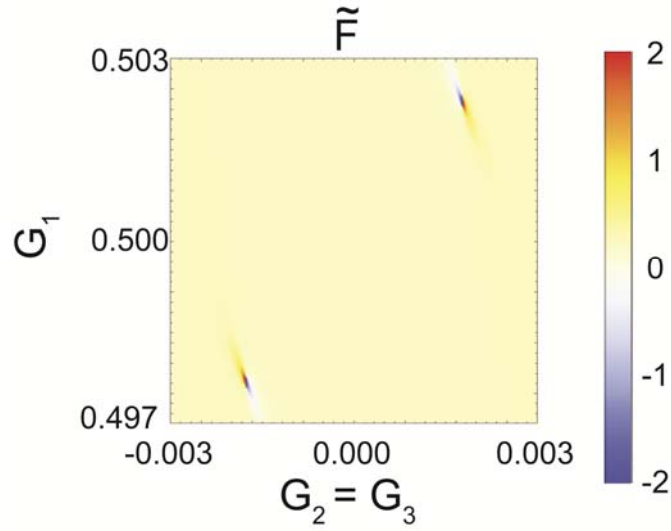
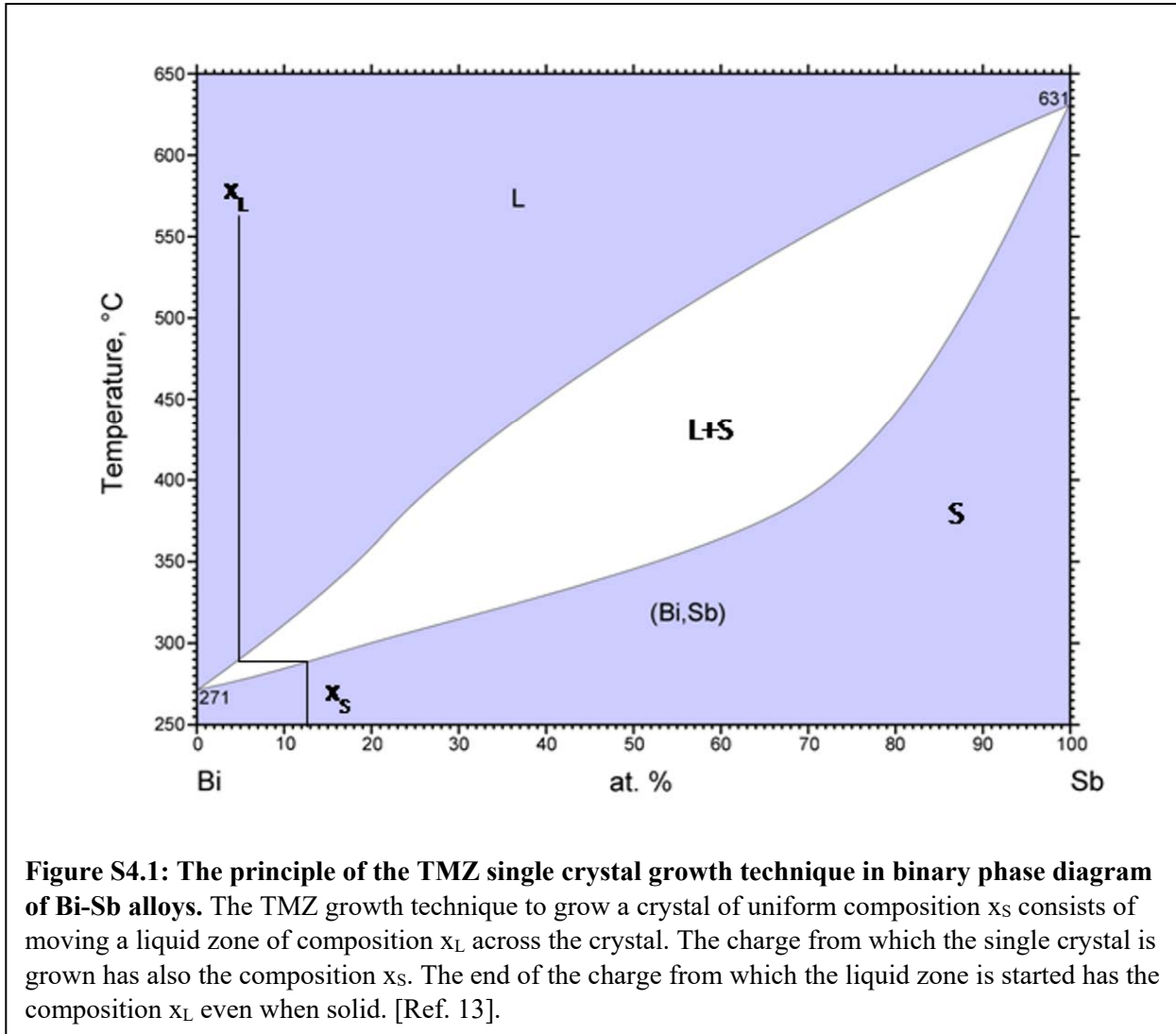


Figure S3.1: Calculated Berry curvature distribution in the G axes system. The coordinates for the separation (1/2 on either side of each L-point) at $H_z = 8$ T for the upper half of the BZ are: (0.678, 0.520, 0.520), (0.520, 0.678, 0.520), (0.520, 0.520, 0.678), in the $G(G_1, G_2, G_3)$ axis system (see **Fig. 1j** in the main text), where (0, 0, 0) is the Γ -point and (0.5, 0, 0) is the L-point along G_1 .

S4. Single-crystal growth and structural characterization.



S4.1 Crystal growth.

High-quality, single crystals of Bi-Sb alloys were grown by travelling molten zone (TMZ) technique,¹² specifically designed to grow crystals with uniform compositions of alloys that form solid solutions, but have very large segregation coefficients, as is the case for the $\text{Bi}_{1-x}\text{Sb}_x$ system. The basic principle is to create a crystal at the composition of the solidus (x_s) from a charge that also has the composition of the solidus x_s , by melting only a small section of the

charge that has the composition of the liquidus (x_L) at the melting point and moving that molten section across the charge (see Fig. S4.1¹³). To obtain a crystal of $\text{Bi}_{88}\text{Sb}_{12}$ ($x_s=0.12$), the composition of the molten zone was maintained at the $\text{Bi}_{97}\text{Sb}_3$ composition ($x_L=0.03$). The bulk of the charge was a $\text{Bi}_{88}\text{Sb}_{12}$ polycrystal, but the leading end, calculated to have the same volume as the molten zone, was a $\text{Bi}_{97}\text{Sb}_3$ polycrystal. According to the binary phase diagram of Bi-Sb, with the $\text{Bi}_{97}\text{Sb}_3$ liquid composition, solid Bi-Sb alloys will start to precipitate out of the liquid phase at the trailing end of the molten zone with a solid-phase composition of $\text{Bi}_{88}\text{Sb}_{12}$. We purchased the starting materials, 99.999 at.% pure Bi and Sb, but in-house Bi zone-refinement before use was necessary to obtain crystals with a low-temperature residual charge-carrier concentration $< 10^{17} \text{ cm}^{-3}$. The traveling speed of the molten zone was set to be 1 mm/hour to ensure equilibrium cooling conditions and avoiding coring. The growth apparatus was horizontal with a free top surface to accommodate the fact that the alloys expand upon solidification.

In practice, while we had aimed for $x_s=12$ at.%, the resulting single crystal had a composition of approximately $x=11$ at%, with an uncertainty and non-uniformity (see below) of composition of 1% over the whole length (80 mm) of the crystal, which was much longer than the samples used for the measurements (typically $5 \times 2 \times 1$ mm). The $\text{Bi}_{85}\text{Sb}_{15}$ crystal was grown using two TMZ passes, under the same circumstances, except that the liquid phase composition contained $x_L=5.8$ at% Sb and the bulk of the charge was a $\text{Bi}_{84}\text{Sb}_{16}$ polycrystal ($x_s = 16$ at.%).

The $\text{Bi}_{95}\text{Sb}_5$ semimetal crystal was grown in-house by the Bridgman technique. A

charge with the

composition of the liquidus

$x_L=5$ at.% was created by

melting a solid mixture of

high-quality elemental

bismuth and antimony at

the desired at.% in the

furnace at $700\text{ }^\circ\text{C}$. The

liquid was then cooled to

$350\text{ }^\circ\text{C}$. The liquid mixture

was cooled slowly at rate

of $0.1\text{ }^\circ\text{C}/\text{min}$ from $350\text{ }^\circ\text{C}$

to $200\text{ }^\circ\text{C}$ in a temperature

gradient induced by natural

convection inside the

furnace. The temperature

gradient cause solid Bi-Sb

alloys to start to precipitate

out of the liquid phase at

the colder end with a solid-

phase composition of $x_S >$

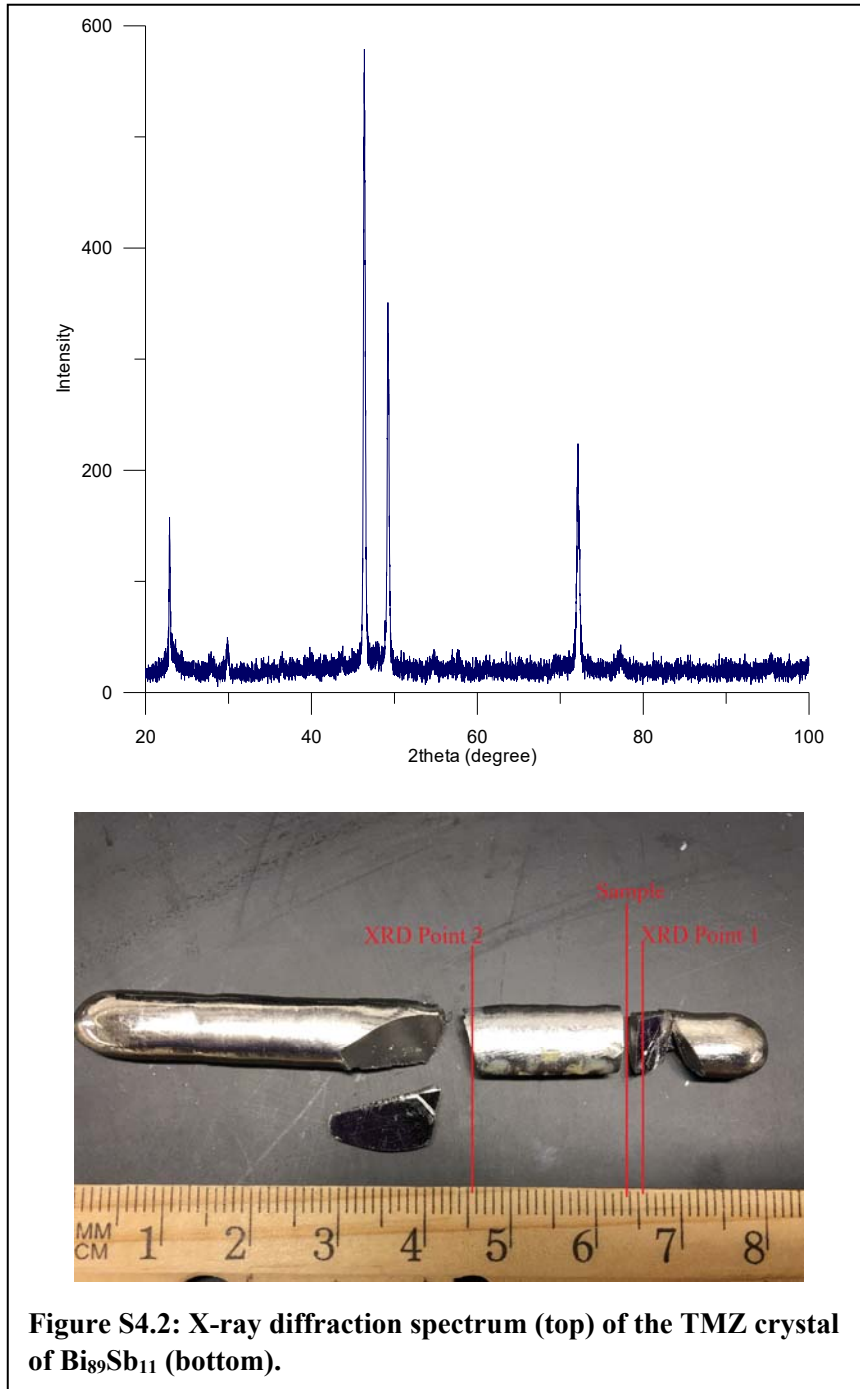


Figure S4.2: X-ray diffraction spectrum (top) of the TMZ crystal of $\text{Bi}_{89}\text{Sb}_{11}$ (bottom).

x_L . As the furnace temperature drops and more solid single crystal forms, the liquidus

composition x_S also drops, creating a composition gradient along the length of the crystal. Slices are cut along the length of the crystal and compositions were checked by X-ray fluorescence (XRF).

S4.2 Crystallography.

The TMZ single crystals (Fig. S4.2) were cleaved revealing shiny, metallic cleavage surfaces. Single-crystal flakes from the cleaved surfaces were collected at the positions marked in Fig. S4.2 on the crystal for characterization using X-ray diffraction (XRD). Si powder was sprinkled on the sample holder and leveled with the exposed surface of the flakes to serve as calibration peaks in the spectrum result (Fig. S4.2). The cleaved surface was confirmed to be the

[001] plane. The Si lines were used to correct small misalignments between sample and XRD spectrometer; the corrections affect the [003] peaks the most, and the [006] peaks, to which they were closest, the least. Therefore, the following calculations

Starting end:					
Si 111	28.4	shift	-0.032	c (Å)	x (%)
Bi 003	22.59	corrected	22.622	11.78223	15.64
Bi 006	46.05	corrected	46.082	11.80869	10.51
Bi 009	71.87	corrected	71.902	11.80852	10.55
				Mean (006,009)	10.53
				St. deviation	0.02
Measured sample (adjacent to starting end):					
Si 111	28.39	shift	-0.042	c (Å)	x (%)
Bi 003	22.55	corrected	22.592	11.79767	12.65
Bi 006	46.05	corrected	46.092	11.80627	10.98
Bi 009	71.84	corrected	71.882	11.81136	10
				Mean (006,009)	10.49
				St. deviation	0.49
Finishing end:					
Si 111	28.41	shift	-0.022	c (Å)	x (%)
Bi 003	22.57	corrected	22.592	11.79767	12.65
Bi 006	46.04	corrected	46.062	11.81354	9.57
Bi 009	71.83	corrected	71.852	11.81563	9.17
				Mean (006,009)	9.37
				St. deviation	0.2

Table S4.1: Uniformity analysis, Bi₈₉Sb₁₁ TMZ crystal.

(Table S4.1) used only [006] and [009] peaks. The composition at each measured position (Fig. S4.2) was calculated by interpolating the measured lattice spacing c (Table S4.1) in the [001] direction with respect to the reported variation of lattice spacing of Bi-Sb alloy in literature.⁷ The accuracy of the measurement of x is the composite of the measurement accuracy (0.49%) and the possible variation in composition across the sample. The latter is approximately 0.1% since the measured sample is 2 mm wide, with a non-uniformity of 1% observed across a 2 cm piece of crystal. The final composition at each position on the sample was 10.5 ± 0.5 at.%, which is rounded off to Bi₈₉Sb₁₁. The difference between the composition aimed for with the TMZ charge (12%) and that obtained (11%) was close to the standard deviation of the measurements.

Single-crystal flakes from the cleaved surfaces of the Bi₈₅Sb₁₅ crystal were collected at positions near the two ends, 45 mm apart, of the crystal for characterization using electron

dispersive spectroscopy (EDS).

Starting end of the Bi ₈₅ Sb ₁₅ single crystal, from which the measured sample was cut			
Element	Net Intensity	Atomic %	Error (%)
Bi	56575.3	84.88	1.1
Sb	3462.3	15.12	4.8
Finishing end of the single crystal			
Element	Net Intensity	Atomic %	Error (%)
Bi	57888.6	82.93	1.11
Sb	4121.6	17.07	4.73

Table S4.2: Uniformity analysis, Bi₈₅Sb₁₅ TMZ crystal.

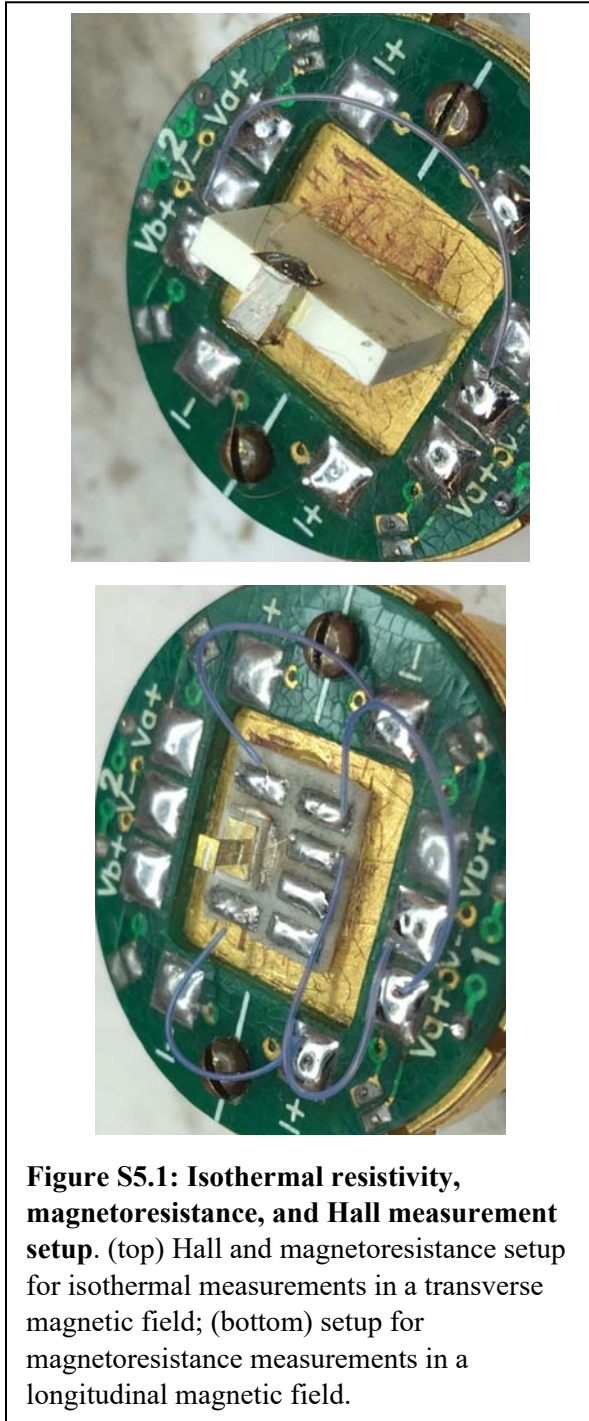
The atomic percentage of Bi and Sb at each position is summarized in the Table S4.2. The characterization measurement accuracy is 0.7 at.% with non-uniformity of less than 2% observed across 45 mm. The sample used for transport measurements is adjacent to the

sample collected at the starting end of the crystal which has composition rounded to Bi₈₅Sb₁₅.

The Bridgeman single crystal was cleaved revealing shiny, metallic cleavage surfaces. The crystal was cut into slices perpendicular to the cleavage surfaces. Composition of each slice was checked by X-ray fluorescence (XRF). The composition of the measured sample was 5 ± 0.5 at.%. The uniformity was checked by interpolating the compositions of adjacent slices which vary from 4.4 ± 0.5 at.% to 5.4 ± 0.5 at.% across a 4mm distance on the crystal, resulting a uniformity of better than 0.5% across the sample size.

S5. Sample characterization: Hall effect, magnetoresistance and thermal conductivity.

S5.1 Sample mount and error bars.



As explained in the main text, five samples originating from three separate single crystals were studied for thermal conductivity: #1 from the TMZ growth of composition $\text{Bi}_{89}\text{Sb}_{11}$, #2, #3 and #4 from the $\text{Bi}_{88}\text{Sb}_{12}$ Czochralski crystal growth by Jacobus Meinhard Noothoven van Goor,¹⁴ and #5 from the TMZ growth of composition $\text{Bi}_{85}\text{Sb}_{15}$. One additional sample (other than those used for thermal conductivity measurements, and on which no electrical contacts were made) from each crystal was subjected to electrical measurements.

The isothermal resistivity and Hall resistivity were measured along the [001] axis of separate samples cut from both the TMZ crystal and the Czochralski crystal using standard Hall bar-geometry setup (5-point probe method), with the magnetic-field direction perpendicular to the electric-field direction. The sample was mounted on a boron nitride block (see Fig. S5.1) that is

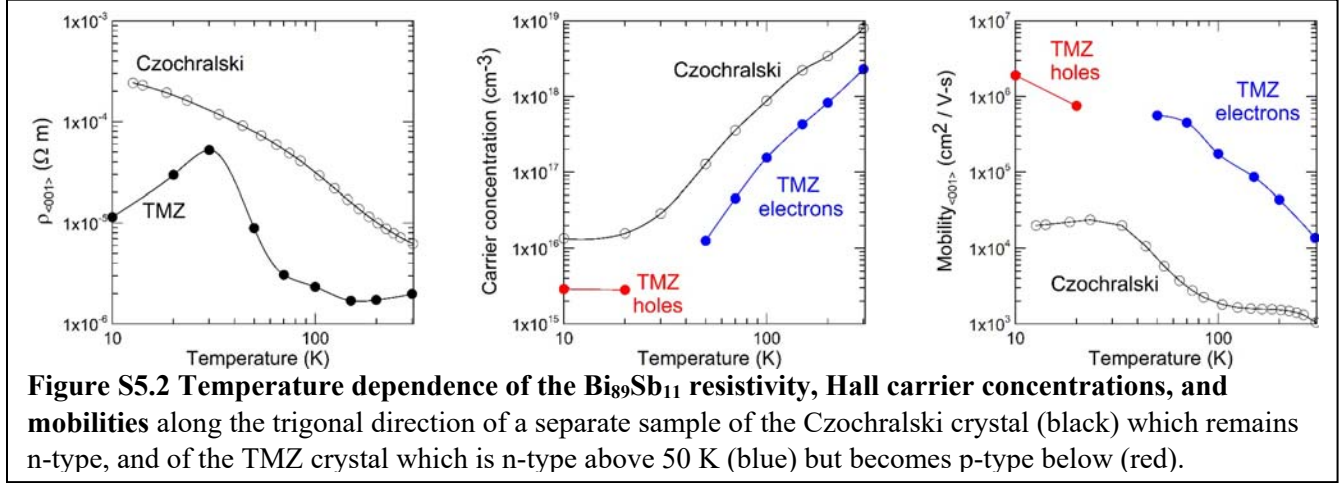
electrically insulating, but thermally conducting. This was done to keep the temperature gradient along the length of the sample negligible, thus negating the effect of secondary Seebeck voltage

and ensuring isothermal measurement conditions.¹⁵ Electrical probing contacts were made with 25 μm copper wires that were spot welded to the sample. Electrical current contacts were made using a current spreader and electrically contacted to the sample with a thin layer of silver epoxy to create an even distribution of current lines. Longitudinal magnetoresistivity was measured on the samples along the [001] crystal axis with the direction of the magnetic field parallel to the electric field. Measurements were conducted at discrete temperature points between 10 K and 300 K. The sample was stabilized thermally at each temperature point for 30 minutes before each measurement was started. Electrical measurements were conducted with direct current and sweeping-down magnetic field from a maximum field of 9 T to a minimum field of -9 T in a Quantum Design Physical Property Measurement System with a sweeping rate of 5 mT/s. Controls software was programmed using LabVIEW.

The error in the high-field Hall and resistivity measurements (i.e., when the product of the mobility times the field is larger than unity, or $H > 5$ mT at 10 K or 50 mT at 100 K) in the transverse magnetic-field setup comes from the geometrical effect. Since the sample is short (L/W ratio is approximately 1.8), at higher field (i.e. $\mu_{mo}B > 1$), the effect of distorted current lines could lead to an underestimation of Hall resistivity by as much as 5 to 10%, as reported in literature.¹⁶

S5.2 Low-field transverse measurements: zero-field resistivity, low-field Hall, carrier concentration, and mobility.

The low-field (i.e., $H < 5$ mT at 10 K and < 50 mT at 100 K) Hall coefficients of $\text{Bi}_{89}\text{Sb}_{11}$ (both TMZ and Czochralski) and $\text{Bi}_{85}\text{Sb}_{15}$ were measured and converted into a carrier concentration, and the low-field mobility then was derived from the resistivity and this carrier concentration. The results are given for both TMZ samples in Fig. 2 of the main text. In Fig.



S5.2., the data on the TMZ and Czochralski samples of composition $\text{Bi}_{89}\text{Sb}_{11}$ are contrasted. The analysis of the data at higher field is given in section S2.

The $\text{Bi}_{89}\text{Sb}_{11}$ TMZ crystal had an electron density and mobility of $2.3 \times 10^{18} \text{ cm}^{-3}$ and $13,700 \text{ cm}^2\text{V}^{-1}\text{s}^{-1}$ at 300 K, and $1.2 \times 10^{16} \text{ cm}^{-3}$ and $559,000 \text{ cm}^2\text{V}^{-1}\text{s}^{-1}$ at 50 K. Below 50 K, the polarity of the Hall effect switched from n-type to p-type, with a concentration and mobility of $3 \times 10^{15} \text{ cm}^{-3}$ and $1,900,000 \text{ cm}^2\text{V}^{-1}\text{s}^{-1}$ at 10 K, indicating an almost complete freeze-out of the charge carriers. A similar behavior is observed in the TMZ- $\text{Bi}_{85}\text{Sb}_{15}$ sample, as reported in Fig. 2 of the main text. The $\text{Bi}_{88}\text{Sb}_{12}$ Czochralski crystals had electron densities and mobilities of $8 \times 10^{18} \text{ cm}^{-3}$ and $1,050 \text{ cm}^2\text{V}^{-1}\text{s}^{-1}$ at 300 K, which froze out to $1.4 \times 10^{16} \text{ cm}^{-3}$ and $20,000 \text{ cm}^2\text{V}^{-1}\text{s}^{-1}$ at 12 K. The fact that the increase in $\kappa_{zz}(H_z)$ was observed on two such vastly different crystals, with low-temperature mobilities varying by a factor 100 demonstrates the robustness of the main result to disorder scattering.

S5.3 High-field longitudinal magnetoresistance effect and error analysis.

As outlined in the main text, the longitudinal magnetoresistance (MR) measurements on WSMs, which generally have electrons of very high mobility, can contain extrinsic signals unless extreme care is taken in sample preparation, dimensions, and alignment. The extrinsic signals can be generated in three ways: current jetting¹⁷, the galvanomagnetomorphic effect^{18,19,20}, and the geometrical MR²¹. Current jetting and the galvanomagnetomorphic effect give rise to an extrinsic negative longitudinal MR, the same sign as would the chiral anomaly. The galvanomagnetomorphic effect is not likely to occur in our samples, first, because their dimensions are orders of magnitude larger than the Larmor radius of the electrons in fields above 1 T, and second, because the data in the main text show the transport to be robust to defect scattering, so that it likely also robust to surface scattering. Current jetting is minimized and checked for by keeping sample dimensions small and placing the voltage contacts at different locations, looking for variations.

The geometrical MR gives rise to an extrinsic positive MR, and arises either when the sample surface is not smooth,¹⁴ or when the field is slightly misaligned with respect to the current flow lines in the sample, as can occur during sample mounting. This is the main cause of difficulties in the present measurements of longitudinal magnetoresistance. The positive geometrical magnetoresistance is given, in general,^{16,21,22} by $\rho_{Geom} = \rho(1 + A\mu_{mo}^2 B_{\perp}^2)$ and the relative correction for the positive geometrical MR is:

$$\frac{\Delta\rho_{Geom}}{\rho} = A\mu_{mo}^2 B_{\perp}^2 \quad (S5.1)$$

where $B_{\perp} = \mu_0 H_{\perp}$ is the magnetic induction in the direction perpendicular to the current and μ_{mo} the mobility and the pre-factor A depends on the ratio between the length of the sample along the current flow direction to its width. The pre-factor varies from $A=1$ for a Corbino disk geometry, to $A=0$ for an infinitely long and thin sample. For the geometries of concern here, there is an uncertainty by almost a factor of 2 on A between the experimental values reported by Weiss and Welker²² on InSb and the calculated values from Wick¹⁶. We therefore cannot use these estimates to calculate a correction term for the MR, so we use A only to calculate an error bar. We adopt the Weiss & Welker values, taking $A=0.05$ for a length-to-width ratio near 10:1. In longitudinal measurements \vec{B} is in theory parallel to the current direction, but in practice field misalignment by an angle θ generates a transverse component $B_{\perp} = |\vec{B}| \sin \theta$ to the magnetic field vis-à-vis the current lines, so that the Lorenz force distorts them. The relative error bar on longitudinal MR measurements is

$$\frac{\Delta \rho_{Geom}}{\rho} = A \mu_{mo}^2 B^2 \sin^2(\theta) \quad (S5.2)$$

In some samples, this error is the main source of error in determining the Lorenz ratio, because it affects the electrical resistivity measurements, but much less the thermal conductivity ones for the reasons outlined in the main text. In sample 6, however, the error (S5.2) is minimized, and the main source of error on the Lorenz ratio at $T > 60\text{K}$ comes from thermal conductivity measurements as discussed in section S10.

S5.3.1 Czochralski samples

MR measurements of the Czochralski crystals contain an additional extrinsic component, identified already by Noothoven van Goor¹⁴. Their surfaces display small striations

in which the current lines are not exactly aligned with respect to the magnetic field. The striations arise because the rotation during the Czochralski growth method results in annular irregularities along the sample length, some 0.05 mm deep on a 3 mm diameter sample. Noothoven van Goor¹⁴ shows how these slight irregularities in the

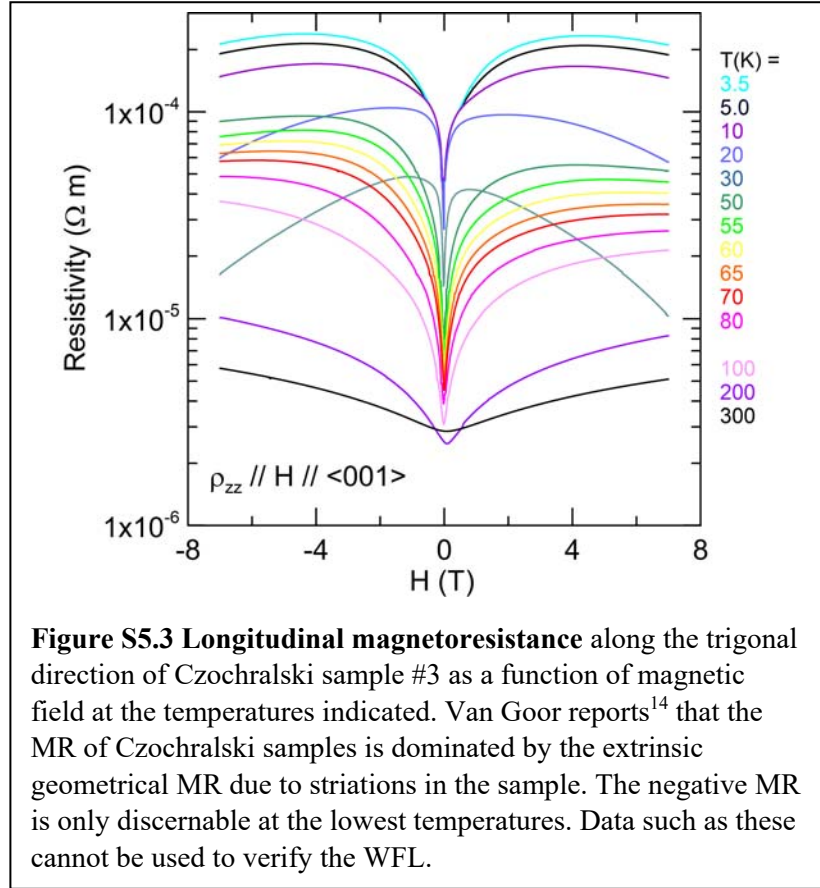


Figure S5.3 Longitudinal magnetoresistance along the trigonal direction of Czochralski sample #3 as a function of magnetic field at the temperatures indicated. Van Goor reports¹⁴ that the MR of Czochralski samples is dominated by the extrinsic geometrical MR due to striations in the sample. The negative MR is only discernible at the lowest temperatures. Data such as these cannot be used to verify the WFL.

sample surface are sufficient to generate an extrinsic geometrical MR. The longitudinal MR of Czochralski Bi₈₈Sb₁₂ crystal sample 3, shown in Fig. S5.3, is uniformly positive at $T > 40$ K, where the increase in κ_{zz} in field is observed. At lower temperature and higher field, the sample develops a negative MR. Due to the difficulties described above, where extrinsic effects can induce either a striation-induced positive or a current-jetting-induced negative MR, it is impossible to attribute either behavior to intrinsic properties of the samples. It is also impossible to verify the WFL law experimentally in a magnetic field on samples with irregular sides.

S5.3.2 TMZ samples

Since both Bi₈₉Sb₁₁ TMZ samples have a high mobility of up to $2 \times 10^6 \text{ cm}^2 \text{V}^{-1} \text{s}^{-1}$ at 10K, the extrinsic positive geometrical MR²¹ that can arise can become an order of magnitude larger

than the intrinsic (negative) sample MR unless extreme care is taken in sample preparation and alignment.

For sample 1, this is illustrated in Fig. S5.4, where the longitudinal MR is given for the same sample in two different geometries: a $\theta = 3.8^\circ$ field misalignment completely eliminates the negative MR. Clearly, no attempt was made to use these electrical data of the 3.35x1.43x1.64 mm sample

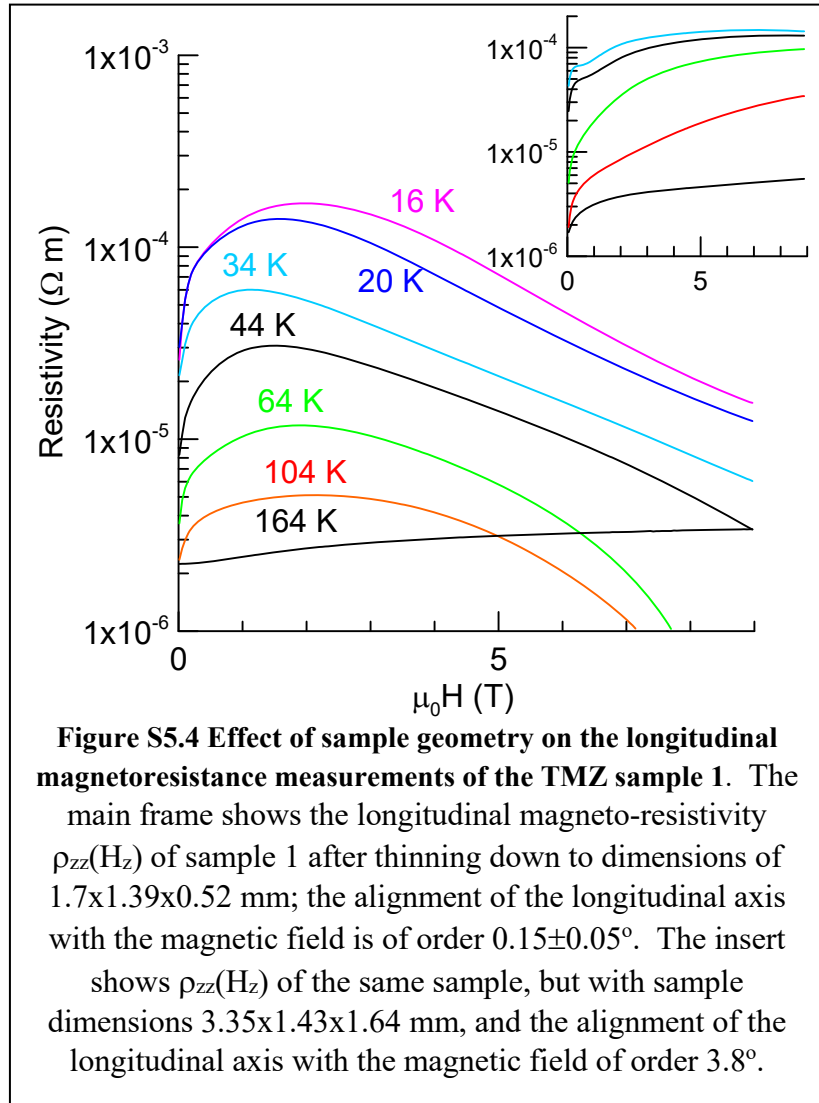


Figure S5.4 Effect of sample geometry on the longitudinal magnetoresistance measurements of the TMZ sample 1. The main frame shows the longitudinal magneto-resistivity $\rho_{zz}(H_z)$ of sample 1 after thinning down to dimensions of 1.7x1.39x0.52 mm; the alignment of the longitudinal axis with the magnetic field is of order $0.15\pm 0.05^\circ$. The insert shows $\rho_{zz}(H_z)$ of the same sample, but with sample dimensions 3.35x1.43x1.64 mm, and the alignment of the longitudinal axis with the magnetic field of order 3.8° .

in any subsequent analysis. The thinned down sample, which was realigned with $\theta = 0.15^\circ$, displays a negative MR with an error bar that will be discussed next. Unfortunately, an attempt at further thinning resulted in the sample cleaving.

Sample 6 was designed specially to minimize all extrinsic effects, as explained in the methods section. The main difference is that mechanical thinning is supplemented by etching, resulting in a smooth surface. The dimensions of sample 6 are 3x0.4x0.6 mm and the misalignment angle was minimized to $\theta = 0.1\pm 0.05^\circ$ by the following process. Two blocks of

BN ceramics were precision cut and glued to the base to serve as precise guides for the sample to stand upright on the platform, with the applied field of Quantum Design PPMS to be

perpendicular to the

platform. These guides

constrain both degrees of

freedom of sample

misalignment. Once the

sample was mounted to the

platform with silver epoxy,

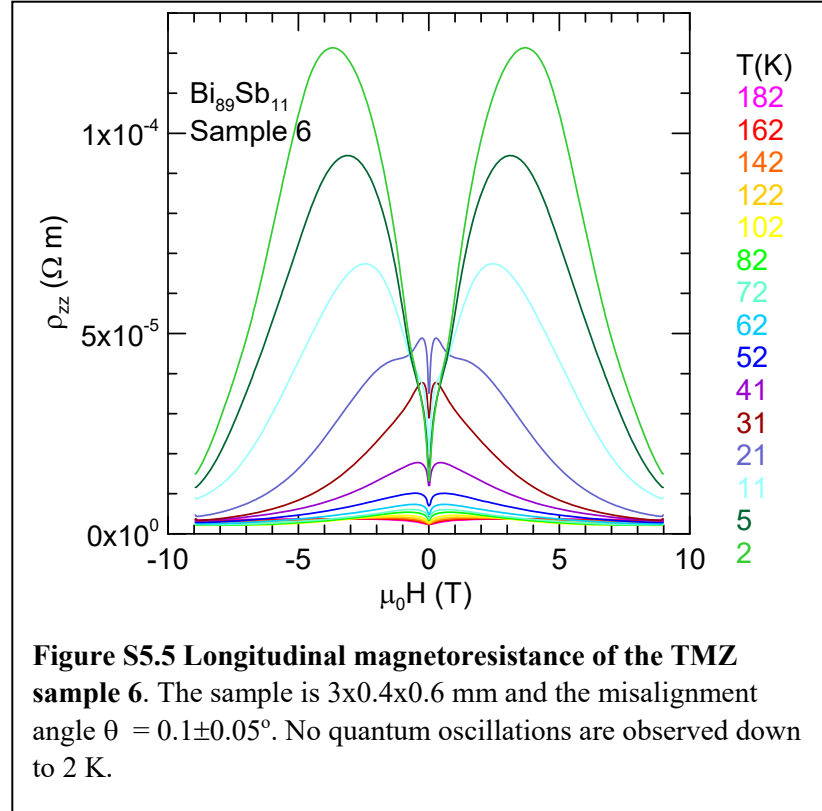
solvents were used to

dissolve the glue and the

guides were removed. The

precision of the guides and

the final alignment were



checked with goniometer (Wixey Model WT41) to be $89.9 \pm 0.05^\circ$. The sample was mounted in a

4 probe geometry. The voltage wires were attached to the sample along the spine of the sample

to minimize effect of current jetting¹⁷. The voltage wires were attached to the sample with a

significant distance from the current wires to avoid regions of large current line distortion. The

measured resistivity $\rho_{zz}(H_z)$ is shown in Fig. 4a. The same data extended to 2 K are shown in Fig.

S5.5. No quantum oscillations are observed even at 2K, as expected from an ideal WSM.

The relative errors in magnetoresistance measurements introduced by the geometry are examined next. The geometries are such²² that for the $3.35 \times 1.43 \times 1.64$ mm sample 1, $A \sim 0.2$ and $\theta = 3.8^\circ$; for the $1.7 \times 1.39 \times 0.52$ mm sample 1, $A \sim 0.25$ and $\theta = 0.15^\circ$; and for sample 6, $A \sim 0.05$

and $\theta = 0.1^\circ$. At 60 K, the mobility of the TMZ Bi₈₉Sb₁₁ crystal is of order of $50 \text{ m}^2 \text{ V}^{-1} \text{ s}^{-1}$. The relative errors for the 3 samples above are thus, at 5 T, a factor of 70, 11% and 1%, and a factor of 3 times higher at 9T.

The error bars increase as the temperature is lowered below 60 K. At 10 K $\mu_{mo} = 2 \times 10^6 \text{ cm}^2 \text{ V}^{-1} \text{ s}^{-1}$ and only sample 6 gives magnetoresistance data that are accurate within 50%. Accurate mobilities are not available in the 30-60K range, due to the fact that the polarity of the Hall effect changes in that range. Since the low-temperature mobility of charge carriers along the trigonal direction of Bi follows a T^2 law²³, it is reasonable to expect that the error bars increase with T^{-4} . Consequently, the determination of the absolute magnitude of the negative magnetoresistance (and thus the Lorenz ratio) cannot be made accurately below 60 K. At 50 K, the error bars given above have already doubled.

S6 Error analysis of thermal conductivity measurements.

The thermal conductivity measurement error has a systematic component that dominates the absolute values of the conductivity reported, and a relative component that dominates the error bars in the temperature and field dependence. The systematic error in the absolute values is composed of a geometric error, an error in the estimate of the heat flux, and an error in thermocouple calibration. The uncertainty of the geometry of the sample is of the order of 10%. Heat losses were calculated from the measured heat leaks of the instrument, which vary with temperature, but are of the order of 1 mW/K at 300 K, smaller than the thermal conductance of the sample. Below 200 K, instrumental heat losses are negligible. The Cu-Constantan thermocouples were calibrated in magnetic field using the process described next and summarized in Table S6.1.

The sensitivity of Cu-Constantan thermocouples used in thermal conductivity measurements of this work has been checked experimentally. The Seebeck coefficients of constituent 25 μm diameter copper and Constantan (Ni-Cu alloy) wires used to fabricate the thermocouples were measured as follows: A temperature gradient was created along the length of a slender piece of glass with one end bonded to a resistive heat source and one end bonded to a heat sink. At steady-state condition, the heat sink temperature is controlled by the temperature controller of Quantum Design PPMS, and the heat flux was constant. At two specific points on the glass, where the ends of the sample wires were welded, temperatures of these points were measured with Cernox[®] temperature sensors that are calibrated in the temperature and field range of the experiment by Quantum Design. The voltage between two ends of the sample wires were measured with a Keithley nanovoltmeter. The measurements were conducted at discrete temperature points between 5 K to 300 K, in sweeping-down magnetic field from maximum field

of 7 T to minimum field of -7 T in Quantum Design PPMS. Controls software was programmed using LabVIEW.

We calculate the Seebeck coefficient of the sample wires using the following formulas:

$$S_{Cu} = \frac{V_{Cu}}{T_H - T_C} - S_M \quad (S6.1)$$

$$S_{Co} = \frac{V_{Co}}{T_H - T_C} - S_M \quad (S6.2),$$

T(K)	S_{TC} at zero field (V/K)	Max. deviation of S_{TC} in field (V/K)	Relative deviation of S_{TC} field (%)	S_{TC} from NBS125 (V/K)	Deviation of S_{TC} from NBS125 (%)
60	1.30E-05	1.33E-05	2.2	1.38E-05	-5.8
40	9.42E-06	1.02E-05	8.1	1.02E-05	-7.3
20	5.33E-06	5.83E-06	9.4	5.50E-06	-3.0
10	2.44E-06	2.62E-06	7.3	3.03E-06	-20

Table S6.1 The thermocouple calibration procedure. The calculated field dependence of Cu-Constantan thermocouples is the difference between columns 2 and 3, given in % in column 4. The total deviation from National Bureau of Standards (NBS) table 125 (data repeated in column 5) is given in column 6.

where V_{Cu} and V_{Co} are the voltages measured between the two ends of sample wires, T_H and T_C are temperatures measured at the two ends of sample wires, and S_M is the Seebeck coefficient of the measuring circuit. Accordingly, we calculate the Seebeck coefficient of the Cu-Constantan couples using:

$$S_{TC} = S_{Cu} - S_{Co} = \left(\frac{V_{Cu}}{T_H - T_C} - S_M \right) - \left(\frac{V_{Co}}{T_H - T_C} - S_M \right) = \frac{V_{Cu}}{T_H - T_C} - \frac{V_{Co}}{T_H - T_C} \quad (S6.3).$$

The resulting values are reported in Table S6.1.

The absolute values of the error, the deviation from NBS reported in the last column, is below 6% down to 60 K, where most of the data are plotted, but can reach 7% at 40 K, and up to 20% below 40 K. Below 20 K, the thermocouples lose their sensitivity, which makes the data noisy, and the calibration errors can reach 20%, which affects the temperature dependence reported in Fig. 3(c) (main text). Combined with the geometric error, the total error at 20 K is 22%. For these reasons, we do not report absolute values for the thermal conductivity below 20 K in Fig. 3(c) (main text). Above 60 K, the total error is 12%, but the relative error on the temperature dependence is below 6%.

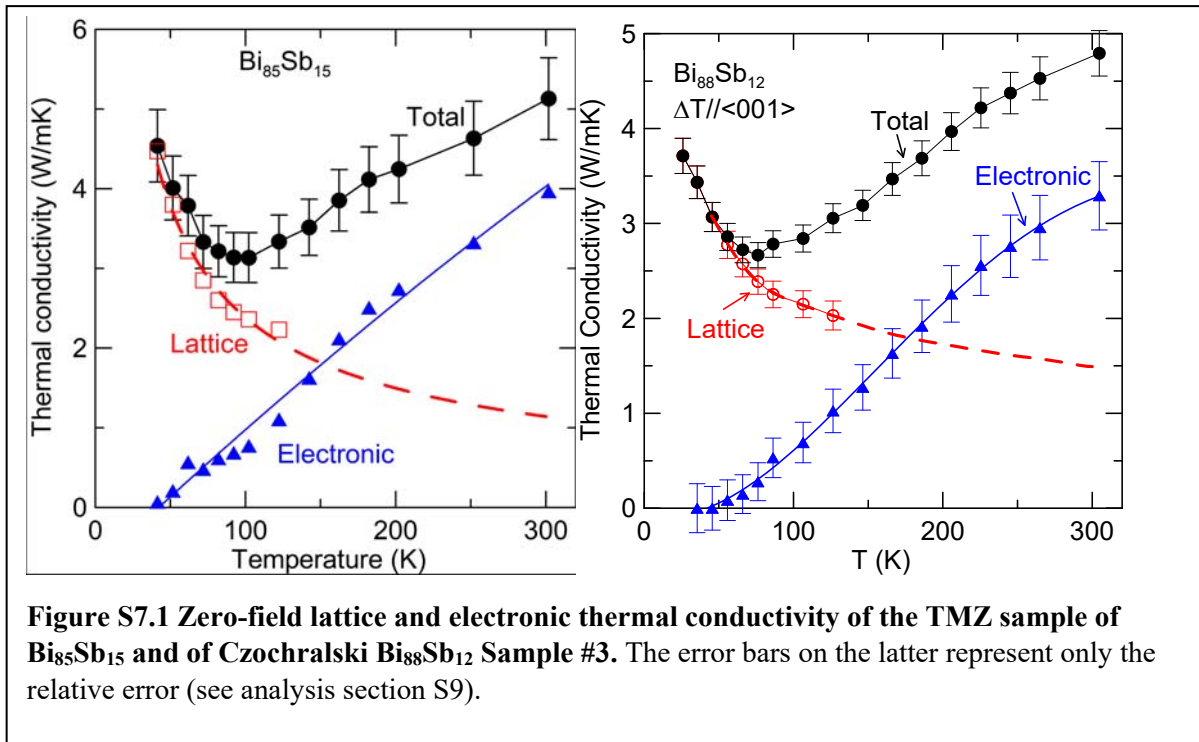
The relative error in the magnetic-field dependence is dominated by the magnetic-field sensitivity of the thermocouples. The dependence on field up to 7 T was checked, is reported in Table S6.1, and is given as error bars in Fig. 3(b) (main text). This uncertainty is less than or equal to 2% down to 60 K, and less than 10% at 34 K, the lowest temperature where the electronic component of κ_{Ezz} is reported. Note that the error bar on the curve at 16 K in Fig. 3(b) (main text) is the only relative error that is relevant to the field dependence; the absolute error, which affects the zero-field value, is much larger and of the order of 25% ($=\sqrt{0.22^2 + 0.1^2}$), as discussed above.

S7 Thermal conductivity κ_{zz} measurements along the trigonal direction.

S7.1 Zero-field conductivity κ_{zz} and its electronic (κ_E) and lattice (κ_L) contributions..

Fig. 2(d) (main text) shows the zero-field thermal conductivity of Bi₈₉Sb₁₁ sample #1.

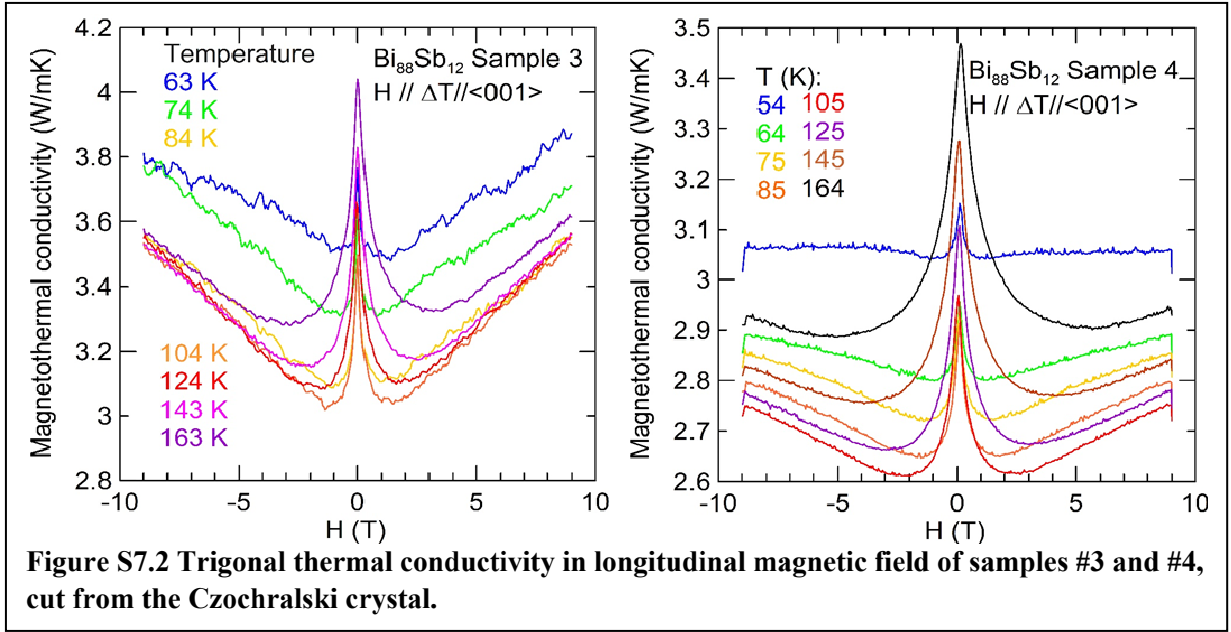
The equivalent figure for the TMZ sample of Bi₈₅Sb₁₅ and of the Czochralski Bi₈₈Sb₁₂ sample #3



is given in Fig. S7.1. The thermal conductivity is separated into κ_L and κ_E by transverse thermal MR measurements described in S7.3.

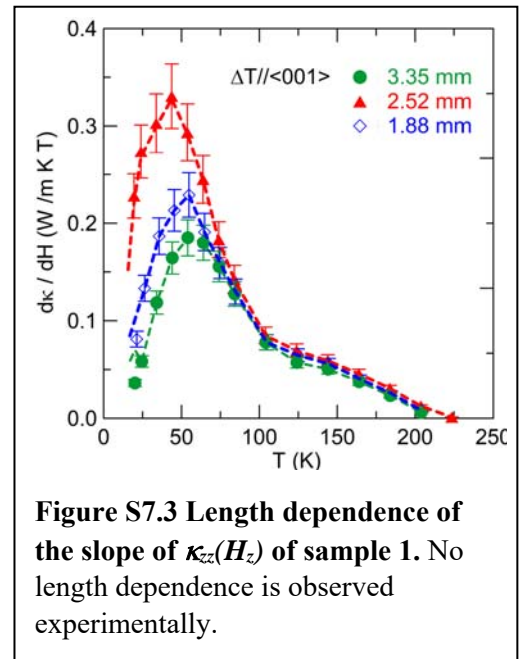
S7.2 Longitudinal magneto-thermal conductivity $\kappa_{zz}(H_z)$: sample-to-sample reproducibility

Besides the sample used for the transverse Hall measurements, three more samples were cut from the Czochralski crystal, with the data on two presented in this section. One (#4) was subjected to a study of the angular dependence of the effect and the data are shown below in Section 8. The zero-field κ_{zz} of sample #3 was analyzed again in terms of an electronic and lattice contribution, as had been done for sample #1 (main text); results are shown in Fig. S7.1.



The $\kappa_{zz}(H_z)$ data on samples #3 and #4 shown in Fig. S7.1 at zero field and in magnetic field have curves are similar to those in Fig. 3 (main text). A region with $d\kappa_{zz}/dH_z > 0$ is visible clearly above a critical field, illustrating the robustness of the effect on impurity scattering, since these samples come from a crystal that has a mobility 100 times smaller than the TMZ samples at 10 K. Czochralski sample #2 shows very similar data, and is described below.

In addition, we examined the sample length dependence of the $d\kappa_{zz}(H_z)/dH_z$ slope of the TMZ $\text{Bi}_{89}\text{Sb}_{11}$ sample #1. The slope, taken at 4.5 T, is shown

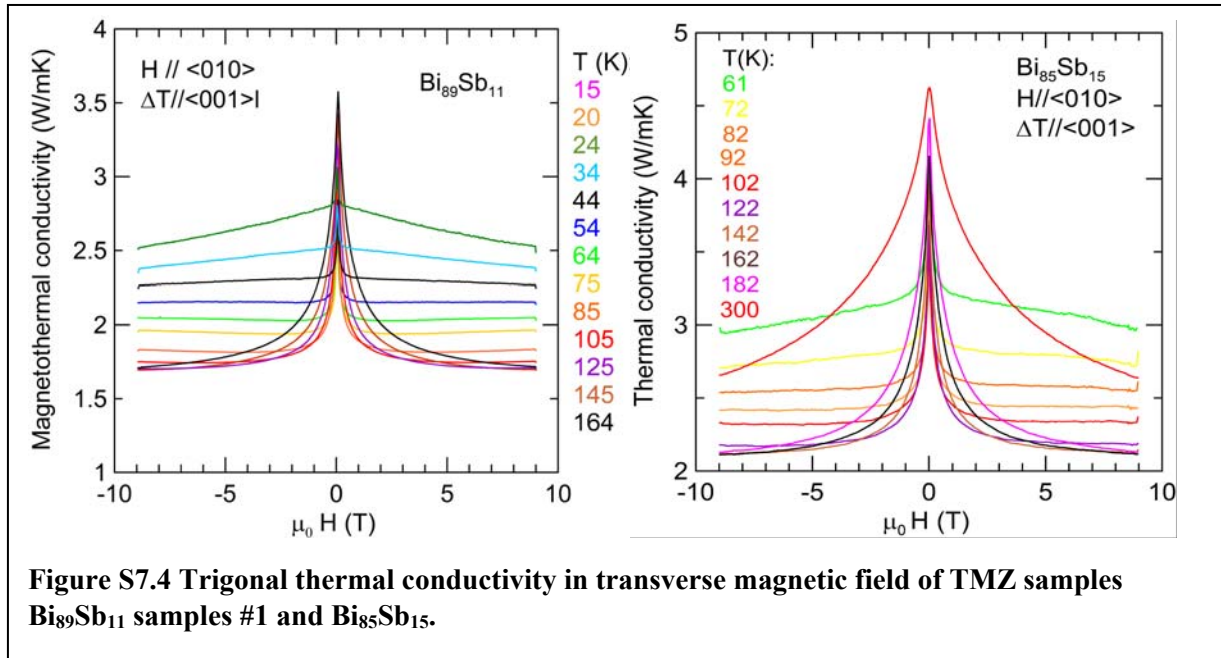


in Fig. S7.3. No length dependence is observed that is significantly above the error bars in the temperature range of the reported results ($T > 60$ K).

For completeness, we mention that anomalously large quantum oscillations in the $\kappa_{zz}(H_z)$ of TaAs²⁴ is interpreted as a manifestation of chiral zero sound. We see no evidence for this behavior in Bi_{1-x}Sb_x ($x > 10\%$) alloys.

S7.3 Transverse magneto-thermal conductivity $\kappa_{zz}(H_y)$.

In the presence of a magnetic field H_y applied along the bisectrix direction $y=[010]$, the thermal conductivity along the trigonal direction, $\kappa_{zz}(H_y)$, decreases monotonically, see Fig. S7.4. This is the ordinary behavior of high-mobility materials such as graphite²⁵ and Bi and $\text{Bi}_{1-x}\text{Sb}_x$



alloys.²⁶ It is used to isolate the lattice term as $\kappa_L = \lim_{H_y \rightarrow \infty} (\kappa_{zz}(H_y))$. The experimental data for $\kappa_{zz}(H_y)$ clearly saturates for $T < 120$ K, and the saturation value is labeled κ_L and plotted as red points in Fig. 2(d) (main text) and Fig. S7.1. At $T > 120$ K, the saturation of $\kappa_{zz}(H_y)$ is not achieved in the fields available, and $\kappa_L(T)$ in Fig. 2(d) (main text) and Fig. S7.1 is extrapolated as a dashed red line following a $T^{-1/3}$ law²⁶ to 300 K. κ_E is taken to be $\kappa_{zz} = \kappa_L$.

S8. Angular dependence of $\kappa_{zz}(H_z)$

As mentioned in the main text and shown in Fig. 4(d) (main text), the angular dependence of the effect was measured on sample #4. $\kappa_{zz}(H_\theta)$ is measured as a function of temperature and magnetic field H_θ applied at an angle θ between the direction of field and temperature gradient in the trigonal direction ($\theta = 0^\circ$ for $H_\theta = H_z$ along $[001]$ plane) / bisectrix direction ($\theta = 90^\circ$ for $H_\theta = H_y$ along $[010]$ plane), as illustrated in Fig.

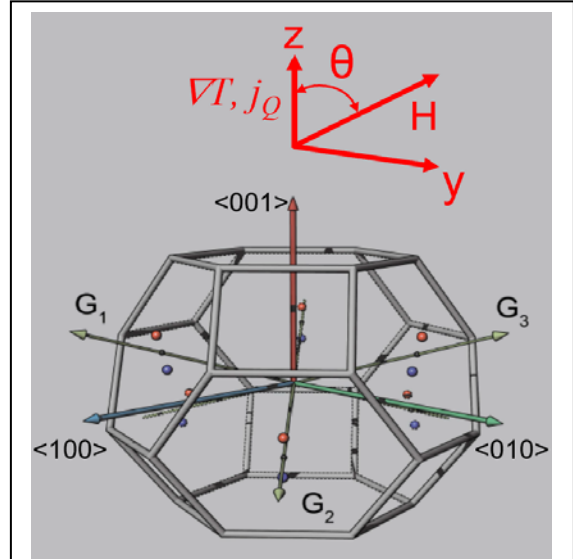


Figure S8.1 Angle between the direction of the magnetic field H_θ and the trigonal axis along which $\kappa_{zz}(H_\theta)$ is measured.

S8.1. The data are summarized in Figure 8.2 and shown as function of both field and angle in Figure S8.3. The value $\Delta\kappa_E = \kappa_{zz}(H = 9\text{T}) - \kappa_{zz,MIN}$, where $\kappa_{zz,MIN}$ is the value of κ_{zz} at the field where it is minimal, is reported in Figure S8.2. The angular dependence follows a $\cos(\theta)^n$ law with $n > 4$, a much higher exponent than expected from the component of H_θ projected along z . Note that sample #2 at $\theta = 0$ again reproduces the data on samples #3 and #4 quite well.

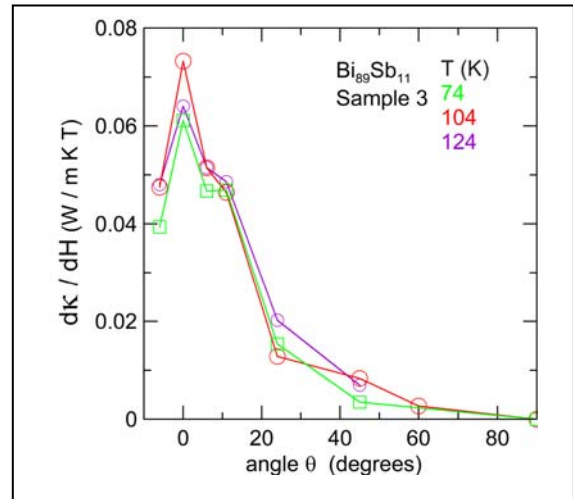


Figure S8.2 Angular dependence of the $\kappa_{zz}(H_z)$ increase. $\Delta\kappa_{zz}$ dependence on angle θ defined as $\theta = 0^\circ$ for $H_\theta = H_z$ along $[001]$, and $\theta = 90^\circ$ for $H_\theta = H_y$ along $[010]$.

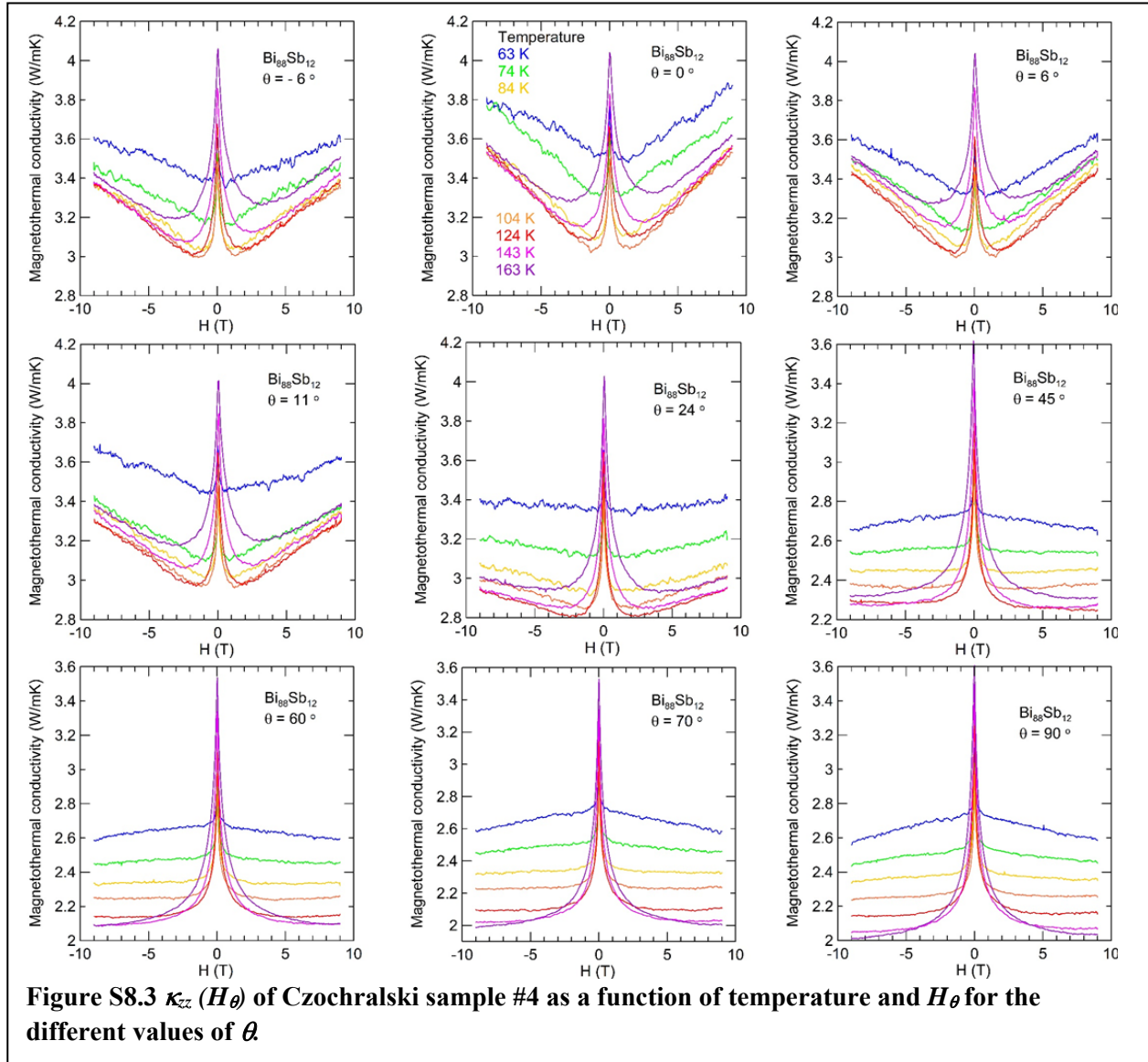


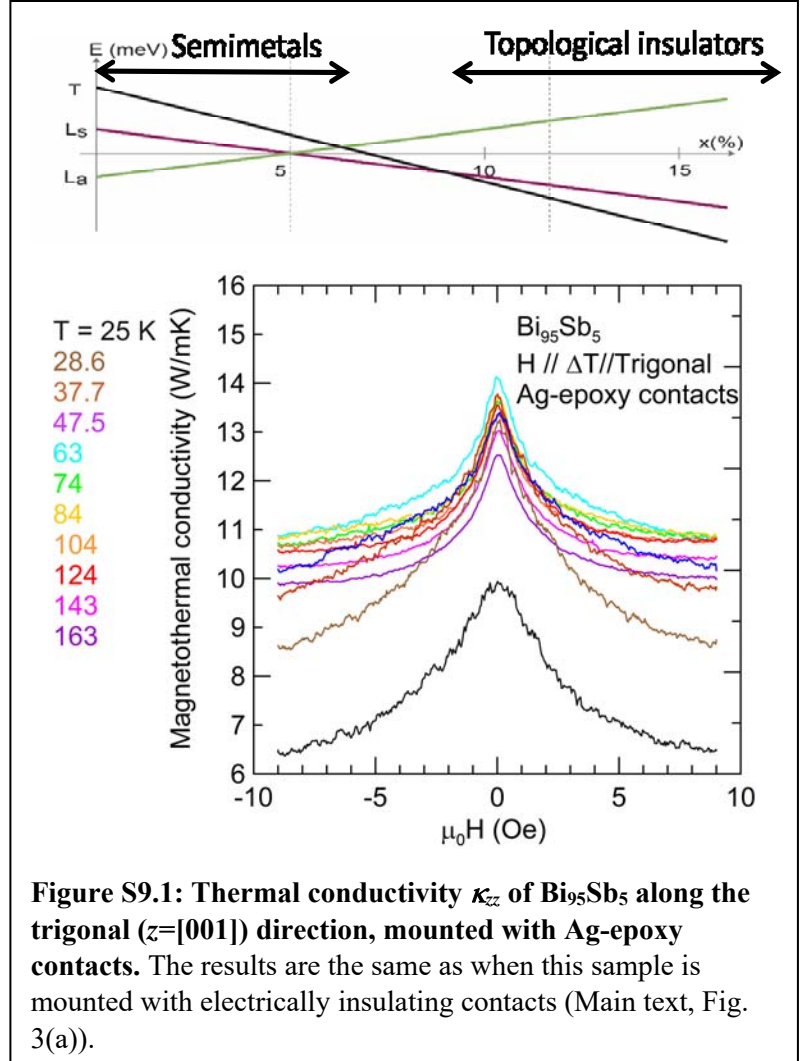
Figure S8.3 $\kappa_{zz}(H_\theta)$ of Czochralski sample #4 as a function of temperature and H_θ for the different values of θ

S9. Test of $\kappa_{zz}(H_z)$ for surface effect.

To test the hypothesis that the increase in thermal conductivity reported in Fig. 3(b-d) (main text) is due to the Weyl nature of the $\text{Bi}_{85}\text{Sb}_{15}$ and $\text{Bi}_{89}\text{Sb}_{11}$ samples studied, the same experiments were carried out on semimetallic samples of $\text{Bi}_{95}\text{Sb}_5$ that are not TIs at zero field, and thus do not move into the Weyl phase at high values of H_z . The $\kappa_{zz}(H_z)$ of this Bridgeman sample (see S4.1) is shown in Fig. 3(a) (main text), and shows $d\kappa_{zz}/dH_z < 0$ at all fields, consistent with the thesis

that $d\kappa_{zz}/dH_z > 0$ is evidence for the chiral anomaly in the Weyl phase. In order to exclude

further the possibility that perhaps the $d\kappa_{zz}/dH_z > 0$ effect might be an extrinsic effect due to surface conduction, a second piece of the same crystal was mounted, this time with electrically conducting Ag-epoxy contacts on the top and bottom surface. The results are unchanged. This



test was also repeated on a piece of the $\text{Bi}_{89}\text{Sb}_{11}$ crystal that showed the positive $d\kappa_{zz}/dH_z > 0$,
and again the Ag coating on the surface had no effect.

S10 Reproducibility of the verification of the Wiedemann-Franz law (WFL) on a second sample.

Figure 4b in the main text shows the verification of the WFL and gives the value for the Lorenz ratio L on sample 6, on which it has been possible to measure the thermal conductivity $\kappa_{zz}(H_z)$ and the electrical resistivity $\rho_{zz}(H_z)$ simultaneously, and on which, per section S5.3, the error on the geometrical magnetoresistance is kept around 3% at $T \geq 60$ K. Whereas the main result of this article, the measurements of the thermal conductivity in longitudinal field, has been reproduced on 6 samples, the verification of the WFL requires accurate and intrinsic measurements of $\rho_{zz}(H_z)$ that are reported only for sample 6. Sample 6 has been thinned by acid etching and mounted using precision-cut guides with an alignment to the field of 0.1° . As explained in section S5.3, $\rho_{zz}(H_z)$ in all samples has extrinsic contributions from geometrical effects, due to sample shape and misalignment, but they are minimized in sample 6. Attempts at eliminating these effects by thinning the other samples resulted in sample breakage. As explained in section S5.3, the geometrical error in the measurements of $\rho_{zz}(H_z)$ is treated as a contribution to its error bar, which contributes to the error bar on L .

In this section, we present WFL verification data in magnetic field on sample 1: while less accurate, they agree with data showed in Fig. 4b. This section uses the $\kappa_{zz}(H_z)$ data of Fig. 4a and the resistivity data of Fig. S5.4. As discussed in S5.3, here the geometrical MR error is of order of 11 - 33% (depending on the field) at $T \geq 60$ K, but could be double that if other values of A are considered. The error becomes prohibitively large at low temperature ($T < 60$ K) where the mobility μ_{mo} is large. The effect of this contribution is to overestimate the resistivity and thus overestimate the Lorenz ratio L .

The determination of the Lorenz ratio as done in Fig. 4b has a second source of error, namely the need to subtract the lattice thermal conductivity κ_L from the measured total. This is done by measuring the thermal conductivity with the field aligned along the bisectrix direction, as explained in section S7.3 For sample 6, we were able to measure all properties on the same sample.

For sample 1, the thermal and electrical data were taken on the same crystal but samples of different sizes and separate measurements. To work around

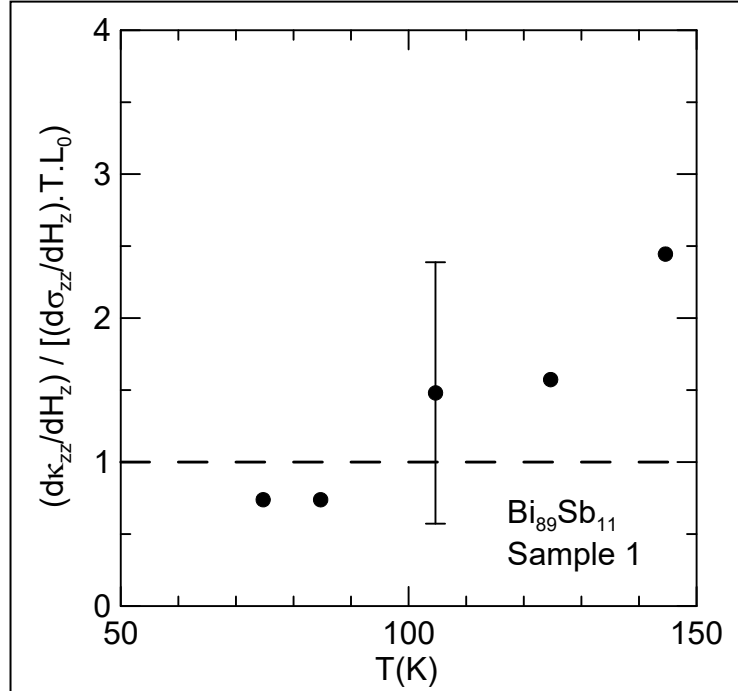


Figure S10.1 Lorenz ratio L/L_0 at $H_z = 6$ T for $\text{Bi}_{89}\text{Sb}_{11}$, sample 1. L/L_0 is here obtained by the derivative method, Eq. S8.1, While less accurate than the values of L/L_0 reported for sample 6 in the main text, the results on sample 1 are consistent with those on sample 6, illustrating the reproducibility of the verification of the WFL in field.

the accuracy problems associated with the subtraction of κ_L , we devised a new method to derive the WFL ratio of sample 1 in the presence of an external magnetic field, based, not on the absolute values of electrical and electronic thermal conductivity (Eq. 4 in the main text) itself, but on their field derivatives. The Lorenz ratio, normalized to L_0 , is then calculated for sample 1 as:

$$L/L_0 = (d\kappa_{zz}/dH_z) / TL_0 (d\sigma_{zz}/dH_z). \quad (\text{S10.1})$$

and is shown in Figure S10.1. Here $d\kappa_{zz}/dH_z$ is taken from the inset to Fig. 4(c) and $d\sigma_{zz}/dHz$ from Fig. S5.4 at 6 T. Because the conductivities change linearly in field from about 4 to 8 T, estimated L is not field-dependent in that range.

The error bar in Fig. S10.1 has a different origin than the error bars in Fig. 4b. It is a combination of three errors. First, the error due to the geometrical magnetoresistance, discussed in section S5.3, is still present. Second, the samples used for Fig. S10.1 were mounted separately for the electrical and thermal measurements, so that the geometric uncertainties associated with the contact placements (about 10%) and sample dimensions affect the measurements in Fig. S10.1; this was not the case for Fig. 4b, where the copper wires of the type-T thermocouples served simultaneously for the electrical and thermal measurements in both field directions. Third, derivative methods have more noise than direct methods. Taken together, and adding the uncertainty on the value of A , the error bar on the determination of the Lorenz ratio on sample 1 in Fig. S10.1 is of the same order of magnitude as the measured value itself.

In summary, while less accurate than the Lorenz ratio obtained by the direct method on sample 6, the results reported in Fig. S10.1 are consistent with the results obtained on sample 6 in the main text, **Fig. 4(b)**.

REFERENCES

- ¹ J. M. Ziman, "Electrons and Phonons", Clarendon Press, Oxford 1960.
- ² Kamal Das, Amit Agarwal, "Thermal and gravitational chiral anomaly induced magneto-transport in Weyl semimetals", *Phys. Rev. Research* **2** 013088 (2020).
- ³ Girish Sharma, Pallab Goswami and Sumanta Tewari, "Nernst and magnetothermal conductivity in a lattice model of Weyl fermions", *Phys. Rev. B* **93** 035116 (2016).
- ⁴ Andreev A. V and Spivak B.Z., "Longitudinal Negative Magnetoresistance and Magnetotransport Phenomena on Conventional and Topological Conductors", *Phys. Rev. Lett.* **120** 026601 (2018)
- ⁵ Liu, Y. and Allen, R. E., "Electronic Structure of the Semimetals Bi and Sb," *Phys. Rev. B* **52**, 1566 (1995).
- ⁶ Teo, J. C. Y., Fu, L., and Kane, C. L., "Surface States and Topological Invariants in Three-dimensional Topological Insulators: Application to $\text{Bi}_{1-x}\text{Sb}_x$," *Phys. Rev. B* **78**, 045426 (2008).
- ⁷ Cucka, P. and Barrett, C. S., "The Crystal Structure of Bi and of Solid Solutions of Pb, Sn, Sb, and Te in Bi," *Acta Cryst.* **15**, 865-872 (1962).
- ⁸ Cho, S., DiVenere, A., Wong, G. K., Ketterson, J. B., and Meyer, J. R., "Transport Properties of $\text{Bi}_{1-x}\text{Sb}_x$ Alloy Thin Films Grown on $\text{CdTe}(111)\text{B}$," *Phys. Rev. B* **59**, 10691 (1999).
- ⁹ Brandt, N., Svistova, E., and Semenov, M., "Electron Transitions in Antimony-rich Bismuth-Antimony Alloys in Strong Magnetic Fields," *Sov. Phys. JETP* **32**, 238 (1971).
- ¹⁰ Putley, D. H., *The Hall Effect and Related Phenomena*, Butterworths, London, 1960.
- ¹¹ Fukui, T., Hatsugai, Y., and Suzuki, H., "Chern Numbers in Discretized Brillouin Zone: Efficient Method of Computing (Spin) Hall Conductances," *J. Phys. Soc. Jpn.* **74**, 1674 (2005).
- ¹² Scherrer, H. and Scherrer, S., "Bismuth Telluride, Antimony Telluride and Their Solid Solutions," p. 211-237 in *CRC Handbook of Thermoelectrics*, D. M. Rowe, Ed., CRC Press LLC, Boca Raton, Florida, 1995.
- ¹³ ASM Alloy Phase Diagram Data Base™, ASM International, <https://matdata.asminternational.org/apd/index.aspx>.
- ¹⁴ Noothoven van Goor, J. M., "Donors and Acceptors in Bismuth," *Philips Res. Rept. Suppl.* **4**, 1-91 (1971).
- ¹⁵ Harman, T. C. and Honig, J. M., *Thermoelectric and Thermomagnetic Effects and Applications*, McGraw-Hill, New York, 1967.
- ¹⁶ Wick, R. F., "Solution of the Field Problem of the Germanium Gyration," *J. Appl. Phys.* **25**, 741-756 (1954).

-
- ¹⁷ Liang, S., Lin, J., Kushwaha, S., Xing, J., Ni, N., Cava, R. J., and Ong, N. P., “Experimental Tests of the Chiral Anomaly Magnetoresistance in the Dirac-Weyl Semimetals Na₃Bi and GdPtBi,” *Phys. Rev. X* **8**, 031002 (2018).
- ¹⁸ Chambers, R. G. “The conductivity of thin wires in a magnetic field”, *Proc. Roy. Soc.* **A202**, 378-394 (1950).
- ¹⁹ Heremans, J. P., Thrush, C. M., Lin, Y-M., Cronin, S., Zhang, Z., Dresselhaus, M. S., and Mansfield, J. F., “Bismuth Nanowire Arrays: Synthesis and Galvanomagnetic Properties,” *Phys. Rev. B* **61**, 2921 (2000).
- ²⁰ Heremans, J. P., Thrush, C. M., Lin, Y-M., Cronin, S. B., and Dresselhaus, M. S., “Transport Properties of Antimony Nanowires,” *Phys. Rev. B* **63**, 085406 (2001).
- ²¹ Baker, D. R. and Heremans, J. P., “The Linear Geometrical Magnetoresistance Effect: Influence of Geometry and Material Composition,” *Phys. Rev. B* **59**, 13927 (1999).
- ²² H. Weiss & H. Welker “Zur transversalen magnetischen Widerstandsänderung von InSb”, *Zeitschrift für Physik* **138** 3220329 (1954)
- ²³ R. Hartman, “Temperature-dependence of the low-field galvanomagnetic coefficients of Bi”, *Phys. Rev.* **181** 1070- 1086 (1969)
- ²⁴ Junsen Xiang, Sile Hu, Zhida Song, Meng Lv, Jiahao Zhang, Lingxiao Zhao, Wei Li, Ziyu Chen, Shuai Zhang, Jian-Tao Wang, Yi-feng Yang, Xi Dai, Frank Steglich, Genfu Chen, and Peijie Sun, “Giant Magnetic Quantum Oscillations in the Thermal Conductivity of TaAs: Indications of Chiral Zero Sound”, *Phys. Rev. X* **9**, 031036 (2019).
- ²⁵ Heremans, J. P., Shayegan, M., Dresselhaus, M. S., and Issi, J-P., “High Magnetic Field Thermal Conductivity Measurements in Graphite Intercalation Compounds,” *Phys. Rev. B* **26**, 3338-46 (1982).
- ²⁶ Kagan, V. D. and Red'ko, N. A., “Phonon thermal conductivity of bismuth alloys,” *Sov. Phys. JETP* **73** (4), 664-671 (1991); translation of *Zh. Eksp. Teor. Fiz.* **100**, 1205-1218 (1991).